TRIUMF

ANNUAL REPORT
SCIENTIFIC ACTIVITIES

2004

MOLECULAR AND MATERIALS SCIENCE

Experiment 782
Non-Fermi liquid behaviour and other novel phenomena in heavy-fermion alloys
(D.E. MacLaughlin, California, Riverside)

Penetration depth in time-reversal symmetry-breaking superconductors

$PrOs_4Sb_{12}$ is a superconductor ($T_c = 1.85\,\mathrm{K}$) with a number of extraordinary properties. It is the only known Pr-based heavy-fermion superconductor, the Pr^{3+} ground state is nonmagnetic, a novel ordered phase appears at high fields and low temperatures, there are multiple superconducting phases, and time-reversal symmetry (TRS) is broken in the superconducting state. Our previous μSR measurements of λ in the vortex state of a powdered sample found evidence for a BCS-like activated dependence at low temperatures, suggesting the absence of gap nodes. But radiofrequency (rf) inductive measurements of the surface penetration depth indicate point nodes in the gap, in disagreement with the μSR results.

We have carried out new μSR experiments on oriented $PrOs_4Sb_{12}$ crystals, and compared μSR and "surface" penetration-depth measurements (e.g., from rf inductance measurements) in $PrOs_4Sb_{12}$ and a number of other superconductors. The discrepancy between these measurements noted above is found in TRS-breaking superconductors but not otherwise, and is therefore correlated with TRS breaking.

Time-differential TF-μSR experiments were carried out at the M15 channel on a mosaic of oriented $PrOs_4Sb_{12}$ crystals. The crystals were mounted on a thin GaAs backing, which rapidly depolarizes muons in transverse field and minimizes any spurious signal from muons that do not stop in the sample. μSR asymmetry data were taken for temperatures in the range 0.02–2.5 K and μ_0H between 10 mT and 100 mT applied parallel to the $\langle 100 \rangle$ axes of the crystals. The data were fitted with the functional form $G(t)\cos(\omega t + \phi)$, where the frequency ω and phase ϕ describe the average μ^+ precession and the relaxation function $G(t)$ describes the loss of phase coherence due to the distribution of precession frequencies. The relaxation rate associated with $G(t)$ is a measure of the width of this distribution and hence of the width δB of the vortex-lattice field distribution.

Neither of the commonly-used exponential or Gaussian functional forms accurately fit the asymmetry data in the normal state, due to μ^+ coupling to both nuclear and Pr^{3+} moments. Data from both the normal and the superconducting states are well fit, however, by either of two slightly more complex functional forms:

the "power exponential"

$$G(t) = \exp[-(\Lambda t)^K],\qquad(1)$$

and the damped Gaussian

$$G(t) = e^{-Wt}\exp(-\tfrac{1}{2}\sigma^2 t^2).\qquad(2)$$

These functions are both phenomenological and have no theoretical motivation. We shall see that the superconducting-state properties obtained from these fits are similar for both functions, which indicates insensitivity to details of the fitting function and justifies *a posteriori* these otherwise arbitrary choices.

Figure 78 gives the temperature dependence of the corrected superconducting-state μ^+ relaxation rates for $\mu_0H = 10$, 20, and 100 mT. It can be seen that the qualitative behaviour of the rates is remarkably independent of the fit function. At 10 and 20 mT both Λ_s and σ_s are nearly temperature-independent below ~ 1 K. At the lowest temperatures the rate is field-independent to within a few per cent between 10 mT and 100 mT. In an isotropic superconductor such as cubic $PrOs_4Sb_{12}$, vortex-lattice disorder is expected to increase the low-field rate; increasing field (increasing vortex density) then decreases the rate as intervortex interactions stabilize the lattice. Thus the field independence of the rate indicates a substantially ordered
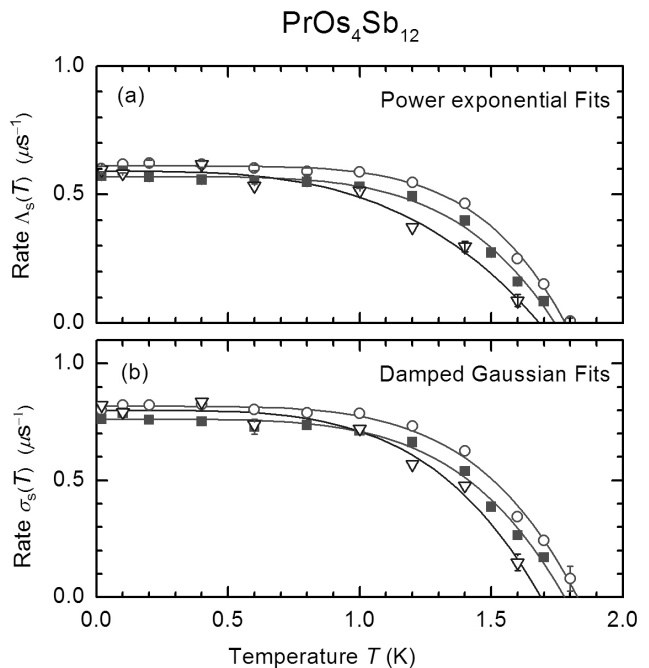

Fig. 78. Temperature dependence of superconducting-state relaxation rates in $PrOs_4Sb_{12}$, corrected for normal-state relaxation (see text). (a) power exponential rates Λ_s. (b) damped Gaussian rates σ_s. Circles: applied field $\mu_0H = 10$ mT. Squares: $\mu_0H = 20$ mT. Triangles: $\mu_0H = 100$ mT. The curves are guides to the eye.

vortex lattice, in which case the temperature dependence of the rate is controlled solely by the temperature dependence of the vortex-lattice field distribution $P_v(B)$. We can also conclude that the field dependence expected as $H \to H_{c1}$ plays no role.

The expression

$$\delta B^2(T) = 0.00371\,\Phi_0^2\lambda^{-4}(T),\qquad(3)$$

where Φ_0 is the flux quantum, relates the second moment δB^2 of $P_v(B)$ to λ for a triangular vortex lattice in the London limit. The second moment of the corresponding μ^+ frequency distribution is $\delta\omega^2 = \gamma_\mu^2\delta B^2$, where γ_μ is the μ^+ gyromagnetic ratio. Then the μSR estimate $\lambda_{\mu SR}$ of the penetration depth from Eq. (3) is

$$\lambda_{\mu SR}\;(\mu m) = 0.328/\sqrt{\delta\omega\;(\mu s^{-1})}.\qquad(4)$$

Now the rms width σ_s of the best-fit Gaussian is not necessarily $\delta\omega$, and replacement of $\delta\omega$ in Eq. (4) by σ_s is not completely justified. Nevertheless σ_s should scale with $\delta\omega$ and, within its range of validity, Eq. (4) should give the correct temperature dependence of $\lambda_{\mu SR}$. This is because under these circumstances effects of nonzero ξ are restricted to the high-field tail of $P_v(B)$, which is not heavily weighted in a Gaussian fit. $PrOs_4Sb_{12}$ is a strongly type-II superconductor (Ginzburg-Landau $\kappa = \lambda/\xi \approx 30$), and this picture should be applicable.

Figure 79(a) compares $\Delta\lambda_{surf}(T) = \lambda_{surf}(T) - \lambda_{surf}(0)$, obtained from rf inductance measurements in the Meissner state, with $\Delta\lambda_{\mu SR}(T)$ obtained using μ^+ relaxation rates for $\mu_0 H = 10\,mT$ in Eq. (4). At low temperatures the difference $\Delta\lambda_{surf}(T) - \Delta\lambda_{\mu SR}(T)$ increases markedly with increasing temperature; this

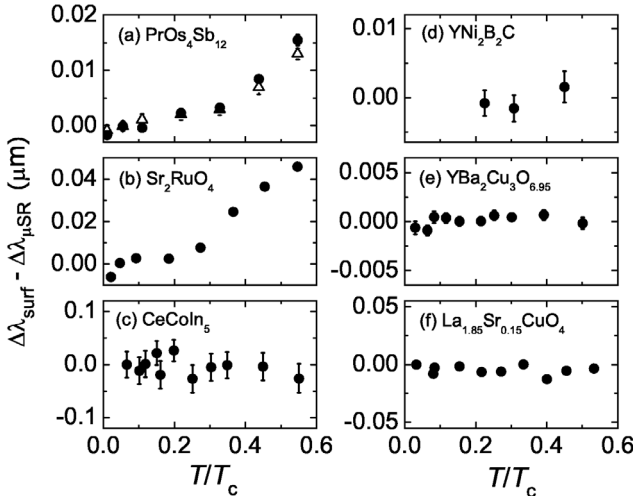Fig. 79. Dependence of difference $\Delta\lambda_{surf} - \Delta\lambda_{\mu SR}$ (see text) on reduced temperature T/T_c in six superconductors. (a) $PrOs_4Sb_{12}$ (this work). Triangles: $\lambda_{\mu SR}$ from Λ_s (Fig. 78(a)). Circles: $\lambda_{\mu SR}$ from σ_s (Fig. 78(b)). (b) Sr_2RuO_4. (c) $CeCoIn_5$. (d) YNi_2B_2C. (e) $YBa_2Cu_3O_{6.95}$. (f) $La_{1.85}Sr_{0.15}CuO_4$.

is the discrepancy between the measurements noted above. It is the same whether $\Lambda_s(T)$ (Fig. 78(a)) or $\sigma_s(T)$ (Fig. 78(b)) is used in Eq. (4); the comparison does not depend on the choice of fitting function. Figure 79(b) gives $\Delta\lambda_{surf}(T) - \Delta\lambda_{\mu SR}(T)$ for the TRS-breaking superconductor Sr_2RuO_4, using data from the literature. Again there is a discrepancy, which is very similar to that in $PrOs_4Sb_{12}$. Small-angle neutron diffraction experiments also found a temperature-independent vortex-lattice field distribution in Sr_2RuO_4 at low temperatures.

Figures 79(c)–(f) give $\Delta\lambda_{surf}(T) - \Delta\lambda_{\mu SR}(T)$ from literature data for the heavy-fermion compound $CeCoIn_5$, the borocarbide YNi_2B_2C, and the high-T_c cuprates $YBa_2Cu_3O_{6.95}$ and $La_{1.85}Sr_{0.15}CuO_4$. None of these superconductors exhibit TRS breaking, and none exhibit the temperature dependence of $\Delta\lambda_{surf} - \Delta\lambda_{\mu SR}$ seen in Figs. 79(a) and (b). There is a significant difference between $\Delta\lambda_{surf}(T)$ and $\Delta\lambda_{\mu SR}(T)$ only for the TRS-breaking superconductors $PrOs_4Sb_{12}$ and Sr_2RuO_4. This is in spite of a wide range of experimental methods and analysis techniques. In Figs. 79(a), (b), (c) and (f) $\Delta\lambda_{surf}$ was obtained from rf measurements, in (d) from magnetization, and in (e) from microwave impedance; in Figs. 79(a) and (c) $\lambda_{\mu SR}$ was obtained from Eq. (4), in (b), (e) and (f) from fits to the expected vortex-state field distribution, and in (d) from a generalization of Eq. (4) to low and high fields.

The origin of this discrepancy and its relation to TRS breaking is not clear. Low-field, low-temperature phase transitions between superconducting states have been reported in both $PrOs_4Sb_{12}$ and Sr_2RuO_4, and may be involved in the discrepancy. The TRS-breaking state may couple to rf or microwave fields, necessitating a revised interpretation of the surface measurements. A mechanism of this sort, in which subgap chiral surface states affect the surface penetration depth, has been proposed for Sr_2RuO_4. A T^2 power law is found for surface measurements even though the bulk energy spectrum is gapped. The theory requires $\lambda \approx \xi$, however, and thus seems inapplicable to $PrOs_4Sb_{12}$. It has also been noted that surface scattering breaks pairs in an odd-parity superconductor. To our knowledge the surface penetration depth has not been calculated taking this effect into account, but pair breaking would decrease the gap and therefore increase the temperature dependence of λ. The discrepancy might be related to a breakdown of the relation $\delta B(T) \propto 1/\lambda^2$ due to nonlinear/nonlocal effects, or to the spontaneous magnetic field in the vortex state (although the measured field is not large enough to have a significant direct effect on δB).

Sr$_2$RuO$_4$ and PrOs$_4$Sb$_{12}$ are both TRS-breaking superconductors but are otherwise very different. Tetragonal Sr$_2$RuO$_4$ is an anisotropic transition-metal-oxide superconductor that is weakly type-II for **H** $\parallel$ **c** ($\kappa_{ab} = 2.3$), whereas cubic PrOs$_4$Sb$_{12}$ is an isotropic strongly type-II heavy-fermion superconductor. The fact that a similar discrepancy between μSR and surface measurements of $\lambda(T)$ is found in such different materials, but not in a variety of non-TRS-breaking superconductors, strongly suggests that TRS breaking is involved.

Experiment 815, 816, 817, 897 and 913
β-NMR
(W.A. MacFarlane, UBC)

The development of β-NMR at ISAC is one of the major efforts at TRIUMF to employ radioactive ion beams in the fields of condensed matter and materials science. These experiments use implanted beta radioactive ions as NMR (nuclear magnetic resonance) probes of local magnetic fields in materials. The beam energies at ISAC are such that 1) the ions penetrate at most a few hundred nanometres (nm) into conventional solids and 2) it is possible to electrostatically decelerate the incident beam (by biasing the target at a high voltage) to vary the implantation depth down to the level of a few nm. Thus many technologically relevant and scientifically interesting phenomena occuring near surfaces and in synthetic thin film heterostructures can be studied with β-NMR. Moreover, there are very few competing depth-resolved probes of such effects. The β-NMR group is pursuing these questions in a variety of materials under several TRIUMF EEC proposals. Some of the recent results in these areas are highlighted below. It should be noted that simultaneously with these measurements, we have been making important technical advances in the instrumentation in order to carry out these measurements with the limited beam time available at ISAC. Some of these are detailed in the last section.

Conventional metals

As part of the initial testing and commissioning of the β-NMR spectrometer at ISAC, we have studied some simple elemental metals, for example silver [Morris *et al.*, Phys. Rev. Lett. **93**, 157601 (2004)]. These measurements are important in establishing the behaviour of the probe in simple materials, for example. There is also fundamental interest in these materials (see Expt. 815 and the new TRIUMF EEC proposal Expt. 1042). As part of this ongoing effort we recently studied a thin film of copper. The behaviour is very similar to that of Au and Ag (reported previously), but the resonances are broader, due to the copper nuclear magnetic dipoles. Similar to Au and Ag, we find a tran-

sition from a cubic interstitial site for the implanted ^{8}Li at low temperature to a substitutional site at higher temperature. The transition occurs at a slightly lower temperature than for Ag (see Fig. 80).

Palladium is another cubic close packed elemental metal which we have previously used to measure ^{8}Li spin relaxation. We have now extended these measurements to the resonances, where we find a remarkably large and negative frequency shift (see Fig. 81). This behaviour is distinct from all the other simple metals we have measured so far and is the subject of active investigation (Expt. 1042).

Niobium is an elemental superconducting metal with the body-centred cubic structure which differs from the cubic close packed structure in that there are no interstital sites of cubic symmetry. Like the other
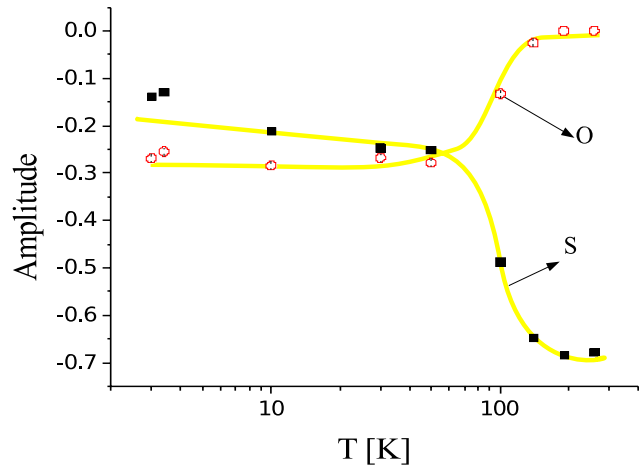

Fig. 80. The resonance amplitudes of the ^{8}Li implanted in a thin Cu film as a function of temperature reflecting the site transition above 100 K, from the octahedral (O) interstitial site to the substitutional (S) site.
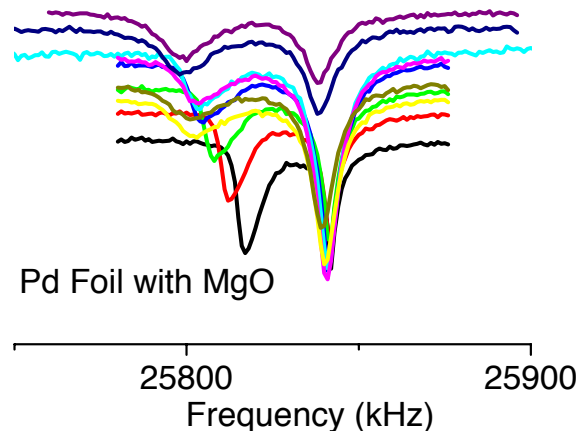

Fig. 81. The resonances of ^{8}Li implanted in a thin foil of Pd as a function of temperature. The foil was wrapped around a crystalline substrate of MgO and pierced with a pin. Centring the beamspot on the pinhole resulted in the composite spectrum including the MgO resonance at the right of the broader Pd resonance.
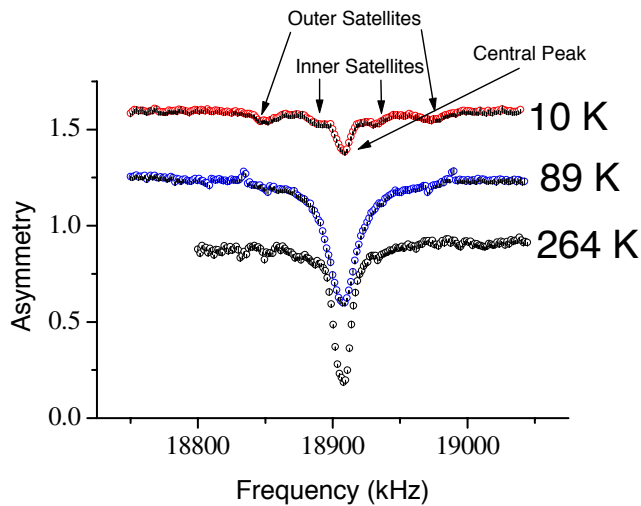
Fig. 82. The resonance of ^{8}Li implanted in an oriented thin film of niobium on a sapphire substrate.

elemental metals we find that the ^{8}Li stops in an interstitial site at low temperature, and at higher temperature it moves to a substitutional site. In niobium this situation is dramatically confirmed as the sites differ in symmetry, and, due to the electric quadrupole moment of the ^{8}Li nucleus, the resonance of the interstitial site is split into quadrupolar satellites (see Fig. 82). This demonstrates the potential to use the quadrupole interaction to identify the ^{8}Li site.

Magnetic heterostructures

As part of Expt. 815, we have been studying a variety of epitaxial metallic heterostructures of iron and silver on GaAs substrates. These kinds of structures are important as they can exhibit giant magnetoresistance and are for this reason used in magnetic storage applications. The effect is a consequence of the depth-dependent magnetic polarization of the nonmagnetic layer by the ferromagnetic layer. A detailed understanding of this polarization (which would represent a significant advance in the field) requires a depth sensitive magnetic probe such as β-NMR.

We have made preliminary studies on several structures of this type, one of which is shown schematically in Fig. 83. This structure had a thick Ag layer deposited on top of a thin magnetic Fe layer. The Ag is then capped with 20 monolayers (4 nm) of Au to protect it. In order to vary the implantation depth the sample was biased to a series of positive voltages. The implantation energy is thus the beam energy minus this bias voltage. In Fig. 84 the resonances are shown at a temperature of 280 K as a function of the bias voltage. The changes in the resonance as a function of voltage clearly show the depth sensitivity of this technique. In particular, at 25 kV the signal is primarily that of unperturbed Ag. At this bias the stopping energy (about
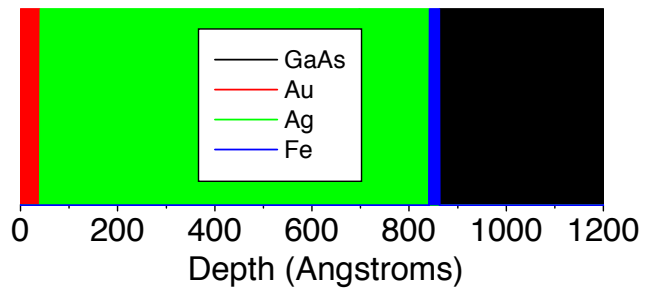

Fig. 83. A schematic of the heterostructure for which a platform bias scan is shown in Fig. 84. The thicknesses are to scale.
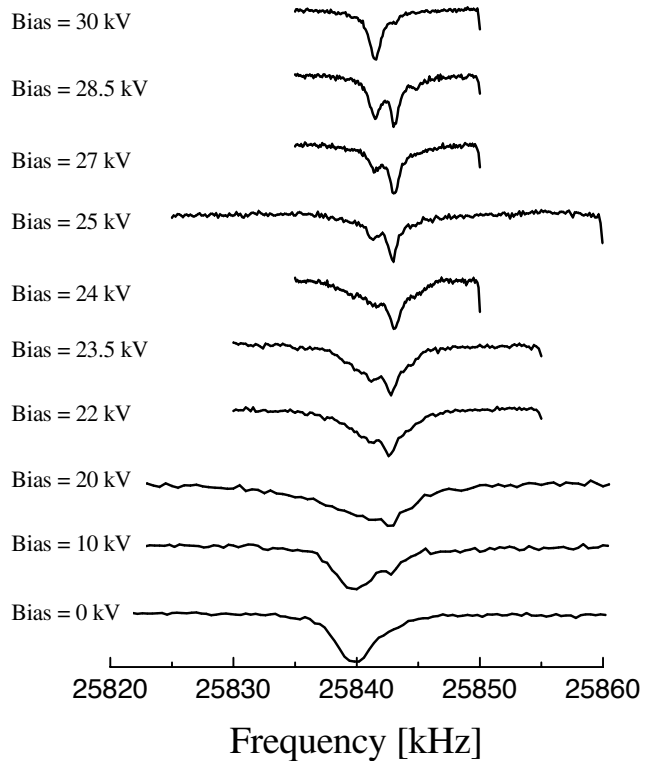

Fig. 84. A bias scan of the ^{8}Li resonances in the heterostructure of Fig. 83 at 280 K. As the bias goes up the implantation energy goes down. The change in the resonance with bias thus demonstrates the depth resolution of the technique.

600 eV) is such that Li stops mainly in the Ag which is too far from the Fe to be perturbed. At the maximum bias (about 100 eV implantation energy), the signal is nearly that of pure gold, i.e. we are stopping all the probe ions in a 4 nm overlayer! This sample is not the ideal geometry to study the polarizing effects of the Fe film, however, so other samples have been and will be studied. One example is shown in Fig. 85. The structure is analogous to that shown in Fig. 83, except the Ag layer is only 20 nm thick. Measurements were taken at room temperature, in an applied external field of 4.5 T, for a range of implantation energies where most of the ^{8}Li stops within the Ag layer. The distribution of
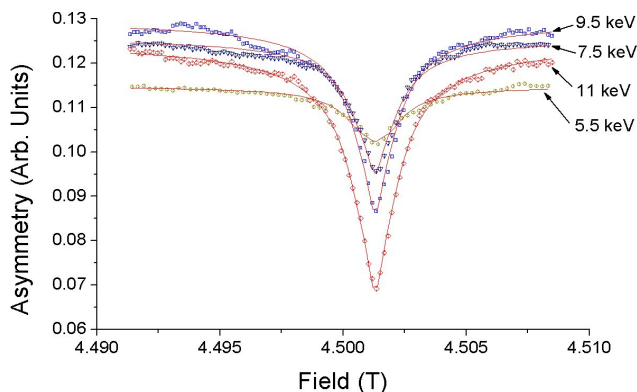
Fig. 85. The resonances as a function of implantation in energy in a thin Fe/Ag heterostructure (see text) – courtesy of T.A. Keeler.

magnetic fields in the Ag layer is reflected in the resonance lineshapes in Fig. 85. The hyperfine coupling is predicted to have an oscillating spatial dependence for a perfectly sharp interface, however, roughness at the interface will introduce random phases that will tend to suppress these oscillations upon averaging over a large lateral area determined by the beam spot, several mm in diameter. Using the stopping distribution of ^{8}Li in the sample, and the form of the hyperfine field decay, it was possible to model the resonance and extract the form of the hyperfine field decay in the Ag layer, which was determined to be a power law $x^{-1.2}$. Detailed analysis is ongoing and will be used to compare with theory and other types of measurements.

Semiconductors

As part of Expt. 816 and Expt. 913 we have been studying high purity crystalline semiconductors. Here the implanted lithium is interesting as an electronically active impurity. Also since these materials are often used as substrates (e.g. for the magnetic heterostructures above) a proper characterization of the β-NMR will be very important for interpreting such measurements correctly.

We have made initial studies of the structure and dynamics associated with ^{8}Li$^+$ in the semiconductors GaAs, Si and Ge. In GaAs (as previously reported) at low temperatures, the amplitude of the ^{8}Li$^+$ resonance indicates that a large fraction (at least 70%) of the Li end up in locations with cubic symmetry (such as the tetrahedral interstitial and substitutional sites). The linewidth of the β-NMR ^{8}Li$^+$ resonance increases dramatically above 150 K, reaches a maximum at about 290 K, and decreases again. This suggests a site-change transition for Li, probably from an interstitial to a substitutional site, at $\approx$150 K, similar to what is found in metals. The picture is similar in germanium, but the line is much narrower at all temperatures, exhibiting only a slight broadening up to room temperature. Additionally, at room temperature there appears a small
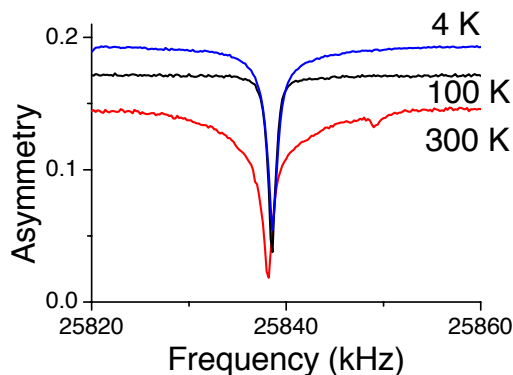
Fig. 86. The resonance of ^{8}Li implanted in a crystal of Ge as a function of temperature.

satellite line shifted to high frequency from the main resonance (see Fig. 86).

Superconductors

The magnetic field distribution in NbSe$_2$ was measured using β-detected NMR of ^{8}Li with a variable implantation energy of 1–30 keV. Figure 87 shows the β-NMR lineshape above and below the superconducting transition temperature ($T_c = 7.0$ K) in a magnetic field of 0.3 T parallel to the hexagonal c-axis. In the normal state at $T = 10$ K a symmetric lineshape is observed with a linewidth attributed to nuclear dipolar

Fig. 87. β-detected nuclear magnetic resonances in NbSe$_2$ above and below the superconducting transition temperature of 7.0 K.

67

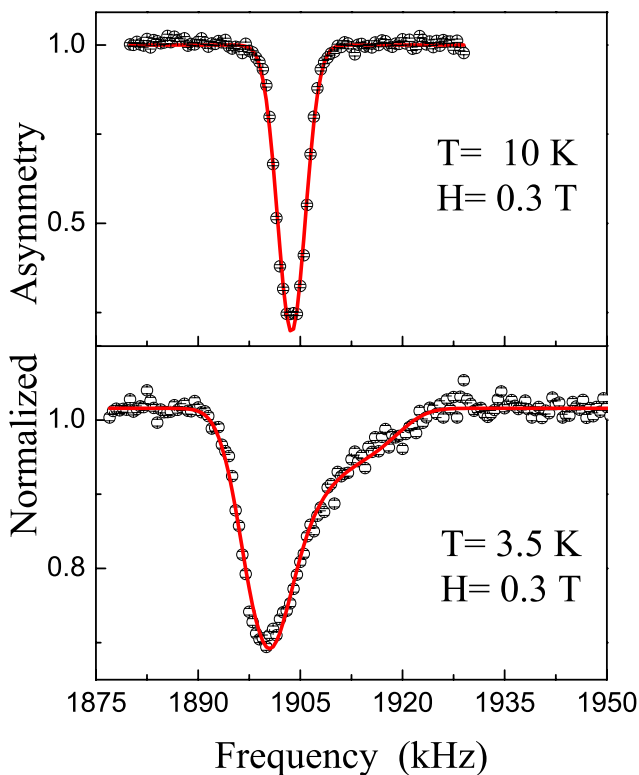broadening from the Nb nuclear moments. Surprisingly there is no evidence for a quadrupolar splitting in the resonance even though $NbSe_2$ is noncubic. At $T = 0.5T_c$ (3.5 K) the characteristic lineshape from a vortex lattice is clearly evident; the peak frequency, from the region between vortices, shifts to a slightly lower frequency and a high frequency develops from the vortex core region. The lineshape was fitted to a modified London model with a Gaussian cutoff function yielding a penetration depth of 272 nm and a coherence length of 12 nm which can be compared with μSR measurements from deeper inside the material. The dependence on implantation energy has also been studied.

While $NbSe_2$ is a very well studied conventional superconductor, its transition temperature is quite low. The recent discovery of high temperature "conventional" superconductivity in MgB_2 may provide another important test case. A preliminary room temperature resonance in a thin film of hexagonal MgB_2 on a sapphire substrate is shown in Fig. 88. The resonance is broad but shows no large quadrupolar effects.

β-detected nuclear quadrupole resonance

As previously reported, the first β-detected nuclear quadrupole resonances (β-NQR) of ^{8}Li at zero field were observed using the newly developed β-NQR spectrometer [Salman *et al.*, Phys. Rev. **B70**, 104404 (2004)]. The resonances were detected in $SrTiO_3$, Al_2O_3 and Sr_2RuO_4 single crystals by monitoring the β-decay anisotropy as a function of a small audio frequency magnetic field (see Fig. 89). The resonances show clearly that ^{8}Li occupies one site with non-cubic symmetry in $SrTiO_3$, two in Al_2O_3 and three sites in Sr_2RuO_4.

The resonance amplitude and width are surprisingly large compared to the values expected due to the transition between $2 \rightarrow 1$ spin states of the ^{8}Li nuclei. The main reason for the enhanced amplitudes is the effect of small, non-axial electric field gradient, which
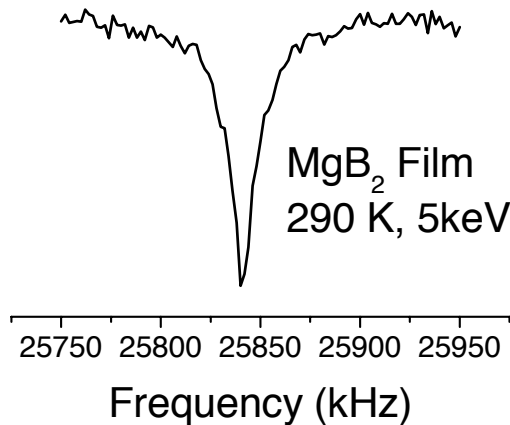

MgB$_2$ Film
290 K, 5keV

Fig. 88. The resonance lineshape of ^{8}Li implanted in a thin film of MgB_2 deposited on a sapphire substrate.
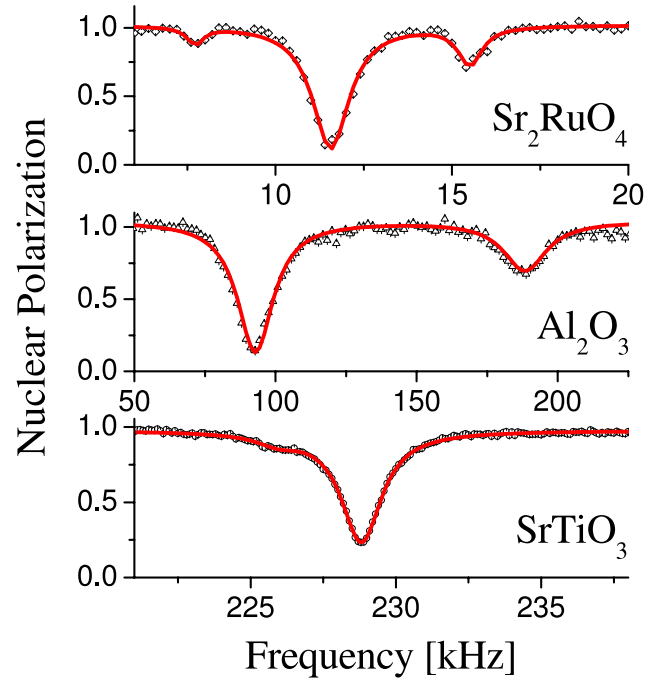
Fig. 89. β-detected nuclear quadrupole resonances in $SrTiO_3$, Al_2O_3 and Sr_2RuO_4 single crystals.

mixes the ± 2 and the ± 1 states, enabling a larger loss of the polarization compared to that expected with vanishing non-axial electric field gradient (i.e. without mixing of the different spin states).

Zero field μSR measurements have proven to be very useful in studies of magnetism. Similarly, we expect that zero field β-NQR will provide a very useful addition for studies of magnetism in thin films and nano-structures.

Summary of technical advances

We have in the past several years transformed the polarimeter station into the β-NQR spectrometer, a second instrument capable of measurements in low fields up to about 150 G. This spectrometer is equipped with its own cryostat and pulsed radio-frequency magnetic system, and we are in the process of designing and implementing a deceleration system similar to the high field platform. We are moving towards near-simultaneous operation of the two spectrometers. For polarization monitoring, we have implemented the "neutral beam monitor" which intercepts the neutral ^{8}Li atoms that are not reionized in the helium vapour cell at the end of the polarizer. Numerous advances have also been made in the data acquisition software, laser polarizer, detector and rf components of the spectrometer. We have also identified problems with ISAC beam stability as well as advanced our understanding of the beam dynamics near the sample. We have *in situ* capability to monitor the beamspot using a sapphire scintillating crystal and a CCD camera. We iden-

tified a problem with discharge electrons produced in the final Einzel lens in the beam line being accelerated and focused by the high magnetic field in the β-NMR spectrometer. We have recently addressed this problem with a negative ring barrier electrode in consultation with M. Olivo. Technical advances such as these will allow us to make maximal use of the scarce ISAC beam time.

Experiment 847
Electron-doped high-T_c superconductors
(J.E. Sonier, F.D. Callaghan, SFU)

All high-temperature superconductors have an insulating antiferromagnetic (AF) phase, and have remnants of this magnetism in the superconducting phase. Determining the role magnetism plays remains the most important fundamental issue in the problem of high-T_c superconductivity. It is still unknown whether magnetism competes or cooperates with superconductivity, and whether these two phases coexist microscopically or are spatially separated. The electron-doped cuprates $R_2Ce_xCuO_{4-y}$ ($R \equiv$ La, Pr, Nd, Eu or Sm) present an interesting situation by having rare-earth moments that strongly couple to the Cu spins residing in the superconducting CuO_2 layers. One purpose of Expt. 847 has been to use the extreme sensitivity of the muon to probe the local magnetic properties of these compounds. The other goal has been to investigate the nature of the low-energy quasiparticle excitations in the vortex state, in an effort to directly address the controversial issue of the symmetry of the pairing state in this class of superconductors. This is a nontrivial task, given that there is no established phase diagram for the vortex state of electron-doped cuprates. In fact, the first direct observation of the vortex lattice in the bulk of an electron-doped superconductor was reported on just this past year [Gilardi *et al.*, Phys. Rev. Lett. **93**, 217001 (2004)]. It is worth noting that prior to this, our own sophisticated analysis of Expt. 847 data determined that the vortex lattice has the square symmetry observed in Gilardi *et al.* [*op. cit.*] by neutrons.

Given that the magnetic exchange interactions in electron-doped cuprates are anisotropic, and that accurate analysis of μSR data in the vortex state must account for all sources of lineshape broadening, it is essential to study single crystals. It is only in recent years that single crystals of reasonable quality have been available in the sizes required for μSR experiments.

The ground state of the Nd^{3+} ion in $Nd_{2-x}Ce_xCuO_4$ is a Kramer doublet, which is split by the interaction with the Cu spins. Doping with Ce introduces itinerant electrons, which are believed to

predominantly occupy the Cu $d_{x^2-y^2}$ orbitals of the adjacent CuO_2 plane. The Ce doping is expected to reduce the magnitude of the Cu-Nd exchange field at the Nd site, thus decreasing the splitting of the Nd-ground state doublet. To further understand the role of magnetism in NCCO, we performed zero-field μSR measurements on an as-grown (non-superconducting) and reduced (superconducting) single crystal with near optimal Ce concentration. The single crystal exhibited a fairly sharp superconducting transition at 23 K.

In the as-grown crystal we determined that there are at least two spatially separated regions with different magnetic character. One of the regions is characterized by slow spin fluctuations, occupying an increasing volume fraction as the temperature is reduced below ~40 K. Below ~6 K, magnetic order is observed (Fig. 90). The other spatial region exhibits fast spin fluctuations down to low temperatures. The temperature dependence of the slow spin-fluctuation volume fraction suggests that the Nd-Nd and Nd-Cu exchange couplings are qualitatively similar to that found in the parent compound Nd_2CuO_4 (in which uniform magnetic order exists). In other words, in a large volume of the sample the exchange couplings are not drastically altered by Ce doping. On the other hand, Ce apparently frustrates magnetic interactions in nearby spatial regions. Thus, the two distinct magnetic regions are most likely due to the disordered spatial distribution of Nd and Ce ions.
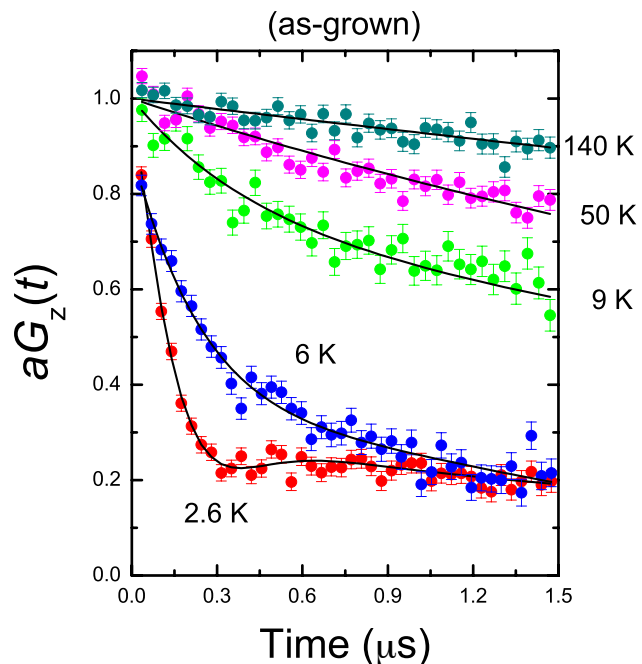

Fig. 90. Temperature dependence of the zero-field μSR asymmetry spectrum of as-grown $Nd_{2-x}Ce_xCuO_4$.
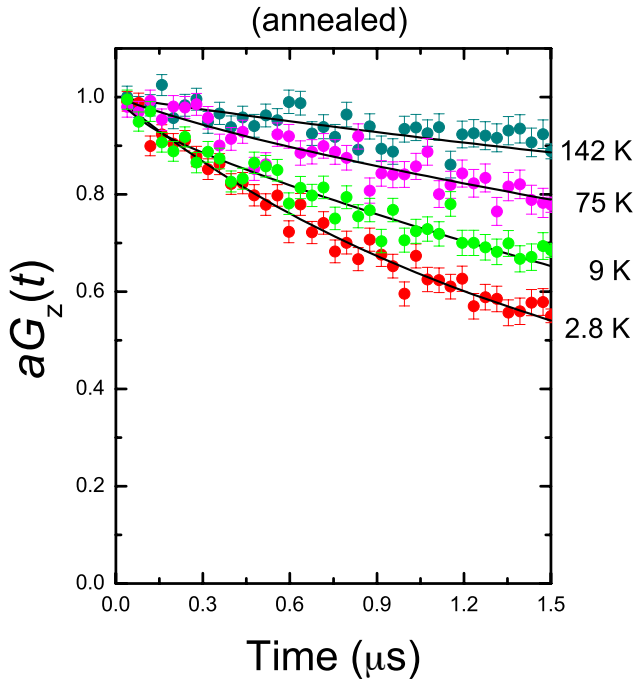
(annealed)

Fig. 91. Temperature dependence of the zero-field μSR asymmetry spectrum of reduced $Nd_{2-x}Ce_xCuO_4$.

Fig. 92. Temperature dependence of the paramagnetic contribution to the lineshape in $Nd_{2-x}Ce_xCuO_4$ at $H = 1$ kG. The curve is a fit to the data assuming a Curie-Weiss temperature dependence.

Recently, it has been determined that reduction of highly doped $Nd_{2-x}Ce_xCuO_4$ creates O(1) vacancies in the CuO2 planes. This is contrary to the widespread belief that the reduction process removes O(3) apical oxygen [Richard *et al.*, Phys. Rev. **B70**, 064513 (2004)]. The O(1) vacancies likely affect long-range AF order. Consistent with this, after annealing the NCCO crystal we observed only fast spin fluctuations throughout the volume of the sample and no magnetic order (Fig. 91).

In transverse-field (TF) μSR experiments on electron-doped cuprates, the rare-earth paramagnetism produces a large muon-spin depolarization rate, proportional to the strength of the applied field and inverse temperature, $1/T$. In the past, this has prevented accurate measurements of the magnetic penetration depth λ_{ab} in the vortex state. The ultimate goal of Expt. 847 is to determine the limiting low-temperature behaviour of λ_{ab}. In 2004, we carried out TF-μSR measurements on the reduced single crystal of $Nd_{2-x}Ce_xCuO_4$ at a field of 1 kG. The field strength was chosen as a compromise between the paramagnetic broadening effects and the vortex density. A considerable amount of time has already been devoted to analyzing the data. The need to account for the paramagnetism of the Nd moments makes the task more difficult than comparable studies on hole-doped cuprates. Even so, at low temperatures we determined that the vortices form a square lattice. While a square vortex lattice is consistent with theories based on $d_{x^2-y^2}$
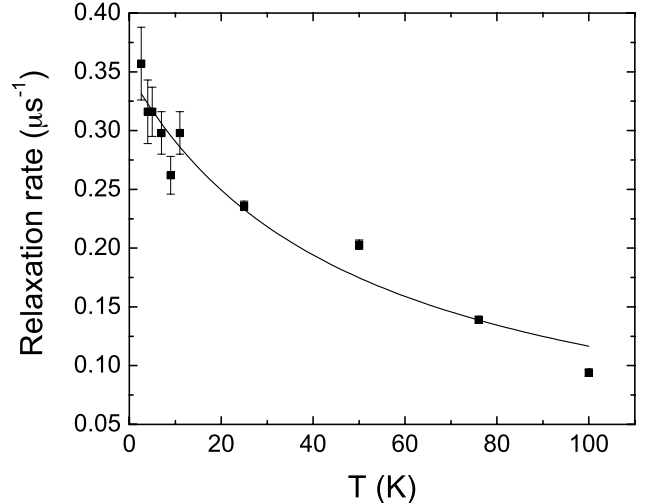
superconductivity, it could also arise from strong coupling to the underlying Fermi surface (as is the case in the conventional s-wave superconductor V_3Si) or other sources of anisotropy. Recently, the square vortex lattice at low fields has been confirmed by neutron scattering [Gilardi *et al., op. cit.*]. The neutron study shows that the vortex lattice at ~ 2.5 K is highly disordered in fields below 0.5 kG and above 2 kG. Thus, it seems our choice of 1 kG was ideal. However, the simplest theory function for the magnetic field distribution of a square vortex lattice contains two additional fitting parameters, and there are additional fitting parameters needed to account for the paramagnetism.

In Fig. 92 we plot the relaxation rate of the term which accounts for the paramagnetism. The data are well described by a Curie-Weiss function indicating that we have successfully extracted the paramagnetic contribution to the μSR lineshape. In Fig. 93 we plot the temperature dependence of the magnetic penetration depth λ determined from our analysis. The data only goes up to $T = 11$ K as the asymmetry of the lineshape decreases at higher temperatures making it more difficult to fit. It can be seen that λ exhibits a steep linear temperature dependence at this field (1 kG). Although the extracted absolute values of λ are very large, a steep linear temperature dependence has recently been observed in the related compound $Sm_{2-x}Ce_xCuO_4$ (SCCO) [Prozorov *et al.*, Phys. Rev. Lett. **93**, 147001 (2004)], the physical cause of which is not yet clear. The behaviour in Fig. 92 may be related to the behaviour in SCCO, and further μSR experiments to investigate this possibility will be undertaken later this year.
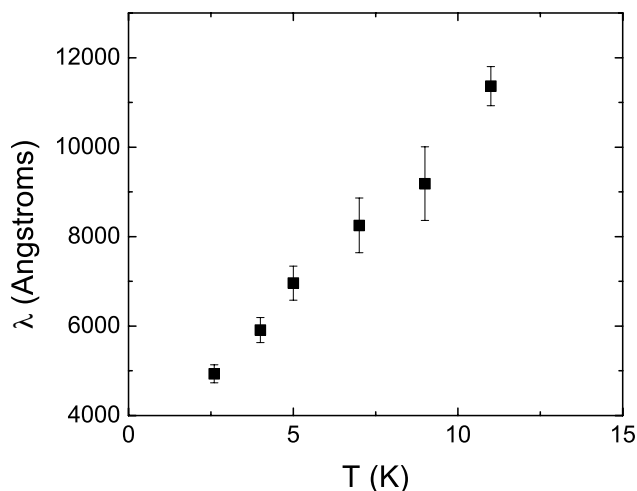
Fig. 93. Temperature dependence of the penetration depth in $Nd_{2-x}Ce_xCuO_4$ at $H = 1$ kOe.

Experiment 917
Correlation between magnetism and transport properties of thermoelectric oxides
(J. Sugiyama, Toyota CRDL Inc.; J.H. Brewer, UBC/TRIUMF)

Recently, a homologous series of $A_{n+2}Co_{n+1}O_{3n+3}$ (A = Ca, Sr, and Ba) was discovered, in which charge carrier transport is restricted mainly to a one-dimensional (1D) CoO_3 chain [Boulahya et al., J. Solid State Chem. **142**, 419 (1999)]. Each chain is surrounded by six equally spaced chains forming a triangular lattice in the ab-plane. As seen in Fig. 94, the CoO_3 chain in the $n = 1$ compound consists of alternating face-sharing CoO_6 trigonal prisms and CoO_6 octahedra. As n increases, only the number of CoO_6 octahedra increases so as to build the chain with n CoO_6 octahedra and one CoO_6 trigonal prism.

The $n = 1$ compound, $Ca_3Co_2O_6$, in particular, has attracted much attention for the past eight years [Aasland et al., Solid State Commun. **101**, 187 (1997); Kageyama et al., J. Phys. Soc. Jpn. **66**, 1607 (1997)]
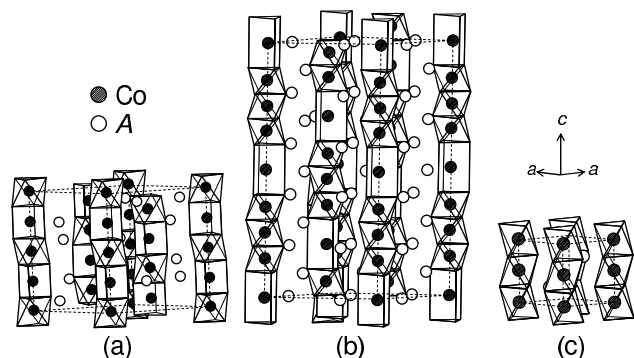

Fig. 94. Structures of the quasi one-dimensional cobalt oxides $A_{n+2}Co_{n+1}O_{3n+3}$ (A = Ca, Sr, and Ba). (a) $n = 1$, (b) $n = 3$ and (c) $n = \infty$.

because it is considered to be a typical quasi-1D system. It was found that $Ca_3Co_2O_6$ exhibits a transition from a paramagnetic to an antiferromagnetic state below 24 K ($= T_N$), although the magnetic structure is not fully understood even after neutron scattering studies, probably due to the competition between the intra-chain ferromagnetic (F) and inter-chain antiferromagnetic (AF) interactions. The valence state of the Co ions was assigned to be +3; also, the spin configuration of Co^{3+} ions in the CoO_6 octahedron is the low-spin (LS) state with $S = 0$ and in the CoO_6 prism the high-spin (HS) state with $S = 2$. At lower temperatures, magnetization and ^{59}Co-NMR measurements suggested the existence of a ferrimagnetic transition around 10 K [Sampathkumaran et al., Phys. Rev. **B70**, 14437 (2004)] which, however, was not seen in the specific heat (C_p) [Hardy et al., Phys. Rev. **B68**, 14424 (2003)]. Furthermore, the C_p measurement revealed an indication of either a short-range magnetic order or a gradual change in the spin state of Co ions at higher temperatures (100–200 K).

The other end member, $BaCoO_3$ ($n = \infty$), crystallizes in the hexagonal perovskite structure, in which the face sharing CoO_6 octahedra form a 1D CoO_3 chain. The chains locate on a corner of the two-dimensional triangular lattice separated by Ba ions [Takeda, J. Solid State Chem. **15**, 40 (1975)]. Although a weak ferromagnetic, ferrimagnetic or spin-glass-like behaviour was observed below ~100 K in the susceptibility [Yamaura et al., J. Solid State Chem. **146**, 96 (1999)], so far there are no reported studies using neutron scattering, NMR or μ^+SR on $BaCoO_3$.

For the compounds with $2 \leq n < \infty$, there are very limited data on physical properties, except for the structural data. Very recently, Takami et al. reported transport and magnetic properties for the compounds with $n = 2$–5 [Takami et al., Jpn. J. Appl. Phys. **43**, 8208 (2004)]. According to their susceptibility (χ) measurements, there are no drastic changes in the $\chi(T)$ curve below 300 K for all these compounds, while the slope of χ^{-1} changes at around 180 K for the compounds with $n = 2$ and 3. As n increases from 1, the Co valence increases from +3 and approaches +4 with increasing n up to ∞; i.e., $BaCoO_3$. Also the ratio between prism and octahedron in the 1D CoO_3 chain reduces from 1/1 for $n = 1$ to 0 for $n = \infty$. Further systematic research on $A_{n+2}Co_{n+1}O_{3n+3}$ is therefore needed to provide more significant information concerning the dilution effect of HS Co^{3+} in the 1D chain on magnetism. In particular, muon spin spectroscopy, as it is very sensitive to the local magnetic environment, is expected to yield crucial data in a frustrated low-dimensional system, as was the case for the 2D layered cobaltites.

71

$n = 1$, 2, 3 and 5 compounds

Figures 95(a)–(c) show the temperature dependences of (a) normalized A_{TF} ($N_{A_{\mathrm{TF}}}$), (b) λ_{TF}, and (c) χ^{-1} in $Ca_3Co_2O_6$ ($n = 1$), $Sr_4Co_3O_9$ ($n = 2$), $Sr_5Co_4O_{12}$ ($n = 3$), and $(Ba_{0.5}Sr_{0.5})_7Co_6O_{18}$ ($n = 5$). The wTF-μ^+SR spectrum below $\sim$100 K was well fitted in the time domain with a combination of three signals; a slowly relaxing precessing signal caused by the applied field, a slowly non-oscillatory and a fast non-oscillatory background signal, namely:

$$
\begin{aligned}
A_0\,P(t) &= A_{\mathrm{TF}}\exp(-\lambda_{\mathrm{TF}}t)\cos(\omega_{\mu,\mathrm{TF}}t+\phi_{\mathrm{TF}}) \\
&+ A_{\mathrm{fast}}\exp(-\lambda_{\mathrm{fast}}t)\,, \\
&+ A_{\mathrm{slow}}\exp(-\lambda_{\mathrm{slow}}t)\,.
\end{aligned}
$$

In order to compare the value of A_{TF} for these samples, $N_{A_{\mathrm{TF}}}$ is defined as $N_{A_{\mathrm{TF}}} \equiv A_{\mathrm{TF}}(T)/A_{\mathrm{TF,max}}$, in which $A_{\mathrm{TF,max}}$ is the maximum value of A_{TF}. Since $A_{\mathrm{TF,max}}$ corresponds to A_{TF} for the paramagnetic state, $N_{A_{\mathrm{TF}}}$ is roughly equivalent to the volume fraction of the paramagnetic phase in the sample.

All four samples show the magnetic transition below 100 K; the onset temperatures of the transition (T_c^{on}) are estimated as 100 ± 25 K for $n = 1$, 90 ± 10 K for $n = 2$, 85 ± 10 K for $n = 3$ and 50 ± 10 K for $n = 5$, respectively. The magnitude of T_c^{on} is thus found to decrease with n. It should be noted that there are no marked anomalies in the $\chi^{-1}(T)$ curve measured with $H = 10$ kOe at T_c^{on} for the four compounds. Although $N_{A_{\mathrm{TF}}}$ for the $n = 1$ compound levels off to its minimum value ($\sim$0) below 30 K, the $N_{A_{\mathrm{TF}}}(T)$ curve for the other three compounds never reaches their minimum even at 1.8 K, indicating that the internal magnetic field is still fluctuating. Indeed, λ_{TF} for the samples with $n = 2$, 3 and 5 increases monotonically with decreasing T, whereas the $\lambda_{\mathrm{TF}}(T)$ curve for $Ca_3Co_2O_6$ ($n = 1$) exhibits a sharp maximum around 55 K.

In spite of the large decrease in A_{TF} below 100 K for the samples with $n = 2$, 3 and 5, the ZF-μ^+SR spectra exhibit no oscillations even at 1.8 K, whereas a clear oscillation is observed in $Ca_3Co_2O_6$. Figures 96(a)–(b) show the muon precession frequency $\nu_{\mathrm{AF}}(= \omega_{\mu,\mathrm{AF}}/2\pi)$ and χ^{-1} in $Ca_3Co_2O_6$. The oscillating signal has a finite intensity below 27 K, while the slow exponential relaxed signal disappears below around 30 K. This

Fig. 95. Temperature dependences of (a) normalized A_{TF}, (b) λ_{TF}, and (c) inverse susceptibility χ^{-1} in $Ca_3Co_2O_6$ ($n = 1$), $Sr_4Co_3O_9$ ($n = 2$), $Sr_5Co_4O_{12}$ ($n = 3$), and $(Ba_{0.5}Sr_{0.5})_7Co_6O_{18}$ ($n = 5$).
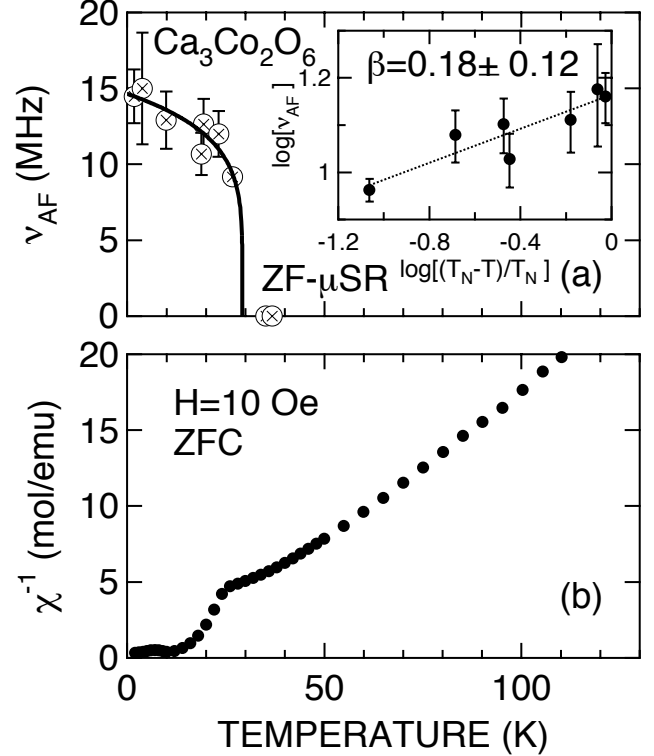

Fig. 96. Temperature dependences of (a) muon precession frequency $\nu_{\mathrm{AF}}2\pi = \omega_{\mu,\mathrm{AF}}$ and (b) χ^{-1} measured in a zero field cooling mode with $H = 10$ Oe in $Ca_3Co_2O_6$.

means that the magnetic moment fluctuating at high temperatures slows down with decreasing T and then orders below 27 K, and becomes quasi-static (within the experimental time scale). The T dependence of ν_{AF}, which is an order parameter of the transition, is in good agreement with the T dependence of the intensity of the AF magnetic diffraction peak determined by a neutron experiment [Aasland *et al.*, Solid State Commun. **101**, 187 (1997)]. Actually, the $\nu_{AF}(T)$ curve is well fitted by the following expression:

$$\nu_{AF}(T) = \nu_{AF}(0K) \times \left(\frac{T_N - T}{T_N} \right)^{\beta}.$$

This provides $\nu_{AF}(0 \text{ K}) = 14.6 \pm 0.8$ MHz, $\beta = 0.18 \pm 0.12$, and $T_N = 29 \pm 5$ K. The critical exponent (β) obtained lies between the predictions for the 2D and 3D Ising models ($\beta = 0.125$ and 0.3125). The value of T_N is also in good agreement with the results of χ and neutron diffraction measurements ($T_N = 24$ K). These results confirm that muons experience the internal magnetic field due to the long-range 2D AF order.

$n = \infty$ compound, $BaCoO_3$

Figures 97(a)–(e) show the temperature dependences of (a) A_{TF}, (b) λ_{TF}, (c) χ^{-1}, (d) specific heat C_p, and (e) its temperature derivative dC_p/dT for $BaCoO_3$ ($n = \infty$). Both A_{TF} and λ_{TF} were obtained by fitting the wTF-μ^+SR spectra, the same way as the compounds with $n = 1$–5. The $\chi^{-1}(T)$ curve indicates the existence of an AF transition at 14 K($= T_N$) with $H = 10$ kOe, but a weak F or ferrimagnetic behaviour below 53 K with $H = 100$ Oe. Also, the $C_p(T)$ curve shows a sharp maximum at 15 K, indicating the existence of a magnetic transition. However, at around 53 K, there are no clear anomalies in the $C_p(T)$ curve, although the slope (dC_p/dT) increases slightly around 50 K with decreasing T. The lack of a clear anomaly around 50 K in the $C_p(T)$ curve suggests that the transition at 53 K is induced by the 1D F order, as in the case for the 1D F order in $Ca_3Co_2O_6$.

The wTF-μ^+SR experiment with 90 Oe shows that as T decreases from 100 K, A_{TF} drops suddenly down to ~ 0 at T_N, indicating that the whole sample enters into an AF state. Such abrupt change in A_{TF} is very different from those for the other quasi-1D cobalt oxides with $n = 1$–5, which typically show a large transition width of 50–80 K. On the other hand, the $\lambda_{TF}(T)$ curve exhibits a small increase below ~ 50 K with decreasing T, probably associated with the complicated magnetism observed in χ with low magnetic fields. As T decreases further from 50 K, λ_{TF} increases rapidly below 17 K, showing typical critical behaviour towards T_N.

The ZF-μ^+SR spectrum at 1.7 K exhibits a clear but complex muon spin oscillation, displayed in

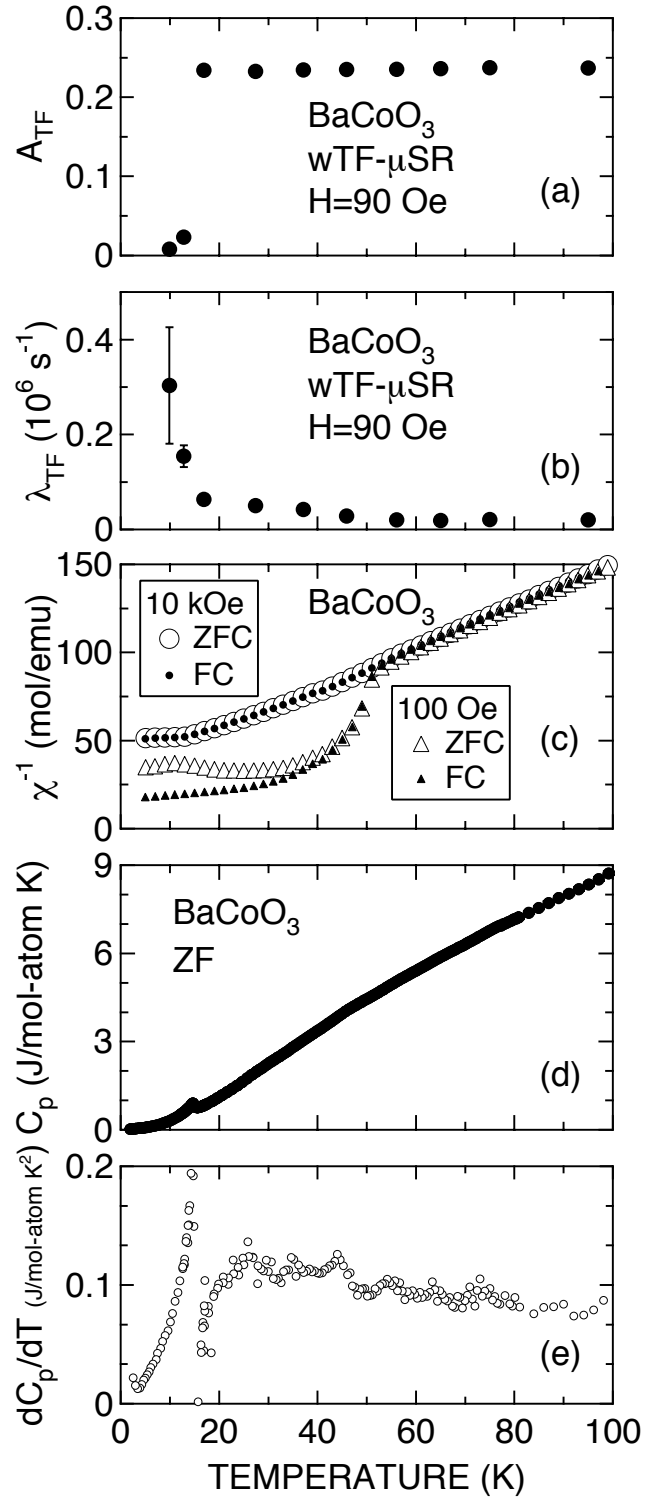

Fig. 97. Temperature dependences of (a) weak transverse field asymmetry A_{TF}, (b) exponential relaxation rate λ_{TF}, (c) inverse susceptibility χ^{-1}, (d) specific heat C_p, and (e) its temperature derivative dC_p/dT for $BaCoO_3$ ($n = \infty$). χ was measured with magnetic field $H = 10$ kOe and 100 Oe in both zero-field cooling (ZFC) and field cooling (FC) mode.
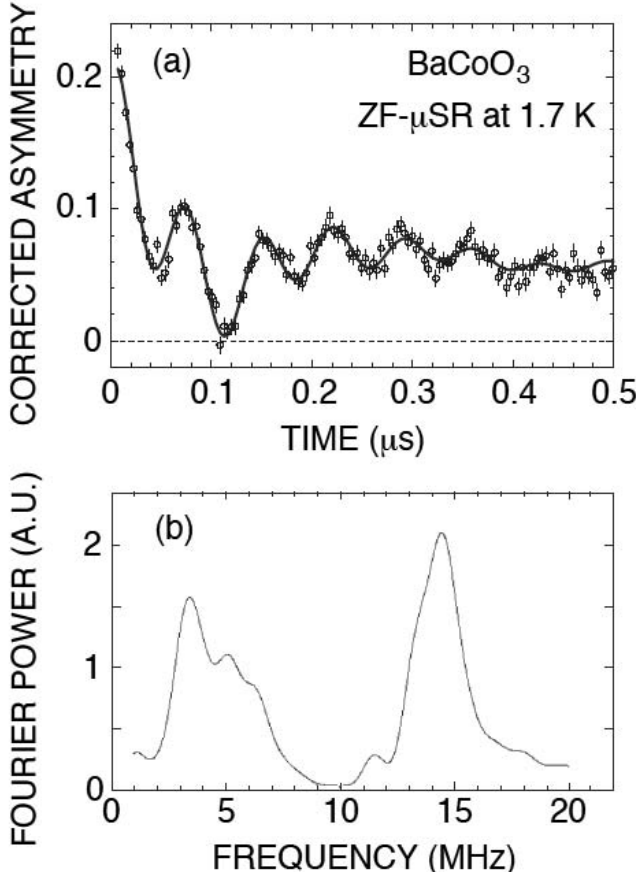
Fig. 98. (a) ZF-μ^+SR spectrum for BaCoO$_3$ ($n = \infty$) at 1.7 K and (b) Fourier transform of (a).

Fig. 98(a). The Fourier transform of the ZF-μ^+SR time spectrum indicates that the ZF-μ^+SR spectrum has five frequency components (ν_μ = 14.4, 13.5, 6.4, 5.1 and 3.5 MHz), even though the sample is structurally single phase at room temperature and there is no indication of any structural phase transition down to 77 K in resistivity (ρ) and thermopower (TEP) measurements; nor are there any anomalies in the $\chi(T)$ curve down to 4 K, except around T_N. The ZF-spectra were well fitted by the following equation:

$$A_0 P(t) = \sum_{i=1}^{5} A_{AF,i} \exp(-\lambda_{AF,i} t) \cos(\omega_{\mu,i} t + \phi)$$
$$+ \sum_{i=1}^{2} A_i \exp(-\lambda_i t),$$

where A_0 is the empirical maximum experimental muon decay asymmetry, $A_{AF,i}$ and $\lambda_{AF,i}$ ($i = 1$–5) are the asymmetries and exponential relaxation rates associated with the five oscillating signals, and A_i and λ_i ($i = 1$ and 2) are the asymmetries and exponential relaxation rates of the two non-oscillating signals (for the muon sites experiencing fluctuating magnetic fields).

Summary

Magnetism of quasi one-dimensional (1D) cobalt oxides $A_{n+2}Co_{n+1}O_{3n+3}$ (A = Ca, Sr and Ba, n = 1, 2, 3, 5 and ∞) was investigated by susceptibility (χ) and muon spin rotation and relaxation (μ^+SR) measurements using polycrystalline samples, at temperatures from 300 K down to 1.8 K. The χ measurement confirmed a systematic change in the charge and spin distribution in the 1D CoO$_3$ chain with n. The weak transverse field (wTF-)μ^+SR experiments showed the existence of a magnetic transition in all five samples investigated. The onset temperature of the transition (T_c^{on}) was found to decrease with n; that is, 100 $\pm$ 25 K, 90 $\pm$ 10 K, 85 $\pm$ 10 K, 50 $\pm$ 10 K, and 15 $\pm$ 1 K for $n = 1, 2, 3, 5$, and ∞, respectively. In particular, for the samples with $n = 2$–5, T_c^{on} was detected only by the present μ^+SR measurements. A muon spin oscillation was clearly observed in both Ca$_3$Co$_2$O$_6$ ($n = 1$) and BaCoO$_3$ ($n = \infty$), whereas only a fast relaxation is apparent even at 1.8 K in the other three samples ($n = 2, 3$ and 5).

A large negative paramagnetic Curie temperature for the samples with $n = 2$ and 3 indicated that the transition at T_c^{on} is caused by an inter-chain two-dimensional (2D) antiferromagnetic (AF) interaction. Considering the structural similarity among the quasi 1D cobalt oxides, the transitions at T_c^{on} for the samples with $n = 1$ and 5 were therefore most likely due to the appearance of the short-range 2D AF order. This suggested that the 1D ferromagnetic order in the CoO$_3$ chain of Ca$_3$Co$_2$O$_6$ ($n = 1$) would occur at higher temperatures ($\sim$200 K) than proposed previously ($\sim$80 K).

For BaCoO$_3$ ($n = \infty$), the χ measurement confirmed that $T_c^{on} = T_N = 15$ K and $T_C = 53$ K, which corresponds to the ferromagnetic (F) transition caused by an intra-chain 1D interaction. Nevertheless, the wTF-asymmetry (A_{TF}) did not exhibit a marked anomaly at T_C, while A_{TF} is very sensitive to the formation of magnetic order. This is likely to be caused by a domain motion in the 1D chain, as in the case for CsCoCl$_3$. In spite of the fact that the sample is structurally homogeneous, the ZF-μ^+SR spectrum showed a complex of at least five frequency components below T_N, which require further detailed studies.

Experiment 932
Improving μ^-SR performance
(J.H. Brewer, UBC/TRIUMF)

The surface μ^+ beams that now dominate most applications of μSR can be "spin-rotated" using Wien filters to orient the muon spins perpendicular to their momenta, thus allowing injection of the beam into arbitrarily high magnetic fields parallel to the momenta

but still perpendicular to the spin polarization. Unfortunately, there are no surface μ^- beams, because negative pions stopping in the production target are immediately captured by positive nuclei. All polarized negative muon beams come from "decay channels" in which the π^- decays in flight. Even "backward" muons generally have higher momentum than the surface μ^+ from π^+ decay at rest, so no "spin rotators" exist for negative muon beams.

In 2004 it was discovered that TRIUMF's M9B superconducting muon channel can be tuned to produce a substantial (roughly 50%) transverse spin polarization in its backward μ^- beam. Although this was not among the new μ^-SR techniques originally proposed for Expt. 932, it represents a significant advance for transverse field (TF)-μ^-SR, one of whose disadvantages relative to TF-μ^+SR has previously been its limitation to weaker transverse magnetic fields.

We have utilized this new capability to make improved TF-μ^-SR measurements of several fundamental phenomena. The magnetic field strength was limited to about 2 T in this experiment by our time resolution of ~ 1 ns (which must be a small fraction of the muon precession period) and by the large radius of the cylinder formed by the electron counters (decay electrons have a radius of curvature of about 5 cm at 2 T and may not reach the detectors at higher fields). Neither of these limitations is intrinsic, but the miniaturization required to go to larger fields conflicts with the sample thickness required to stop backward muons, so it would be difficult to work at fields higher than about 5 T.

Relativistic shifts of g_μ in muonic atoms

A lepton bound in a deep Coulomb potential experiences a relativistic shift of its spin precession frequency in a magnetic field. This effect was first calculated by Breit in 1928 assuming pointlike nuclei, and later improved upon by Margeneau and later by Ford *et al.* in papers accompanying the first experimental measurements of such shifts for negative muons. Subsequent measurements of bound μ^- frequency shifts were made by Yamazaki *et al.* in heavier muonic atoms where the finite size of the nucleus is comparable to the mean radius of the muon wavefunction, causing the relativistic shift to level off toward a constant value as a function of atomic number. Since then there have been few measurements or calculations, except for some recent experiments by Mamedov *et al.*, in which Yamazaki's experimental result for Cdμ^- atoms was called into question.

We have now remeasured many of these shifts in a 2 T magnetic field. The "raw" fitted frequencies are given in Table XIV.

Table XIV. Measured frequencies in a constant magnetic field. Only statistical uncertainties are exhibited in this table, to illustrate that the potential accuracy of this technique is much higher than we have achieved in this modest effort.

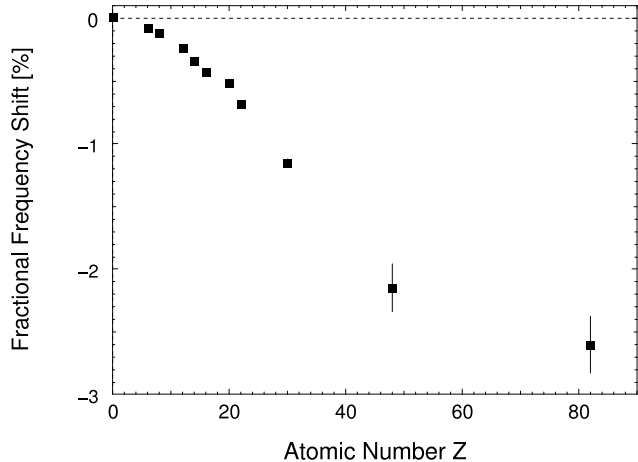| Sample	Frequency (MHz)
μ^+ in graphite	271.69888 ± 0.00072
μ^+ in Al metal	271.58520 ± 0.00038
μ^- on ^{12}C (graphite)	271.3684 ± 0.0016
μ^- on ^{16}O (H$_2$O)	271.258 ± 0.010
μ^- on ^{24}Mg (metal)	270.9259 ± 0.0027
μ^- on ^{28}Si	270.6502 ± 0.0069
μ^- on ^{32}S (powder)	270.406 ± 0.008
μ^- on ^{40}Ca (metal)	270.164 ± 0.069
μ^- on Ti (metal)	269.719 ± 0.066
μ^- on Zn (metal)	268.440 ± 0.072
μ^- on Cd (metal)	$265.73^{+0.46}_{-0.57}$
μ^- on Pb (metal)	$264.50^{+0.59}_{-0.62}$

Fig. 99. Fractional shifts of bound μ^- spin precession frequencies in various muonic atoms, relative to the μ^+ precession frequency in vacuum, assuming a μ^+ Knight shift of $+80 \pm 4$ ppm in Al, which was used as a reference.

All samples were measured in a transverse magnetic field of 2 T. Unlike those in Table XIV, the error bars shown in Fig. 99 include all known systematic uncertainties, but not diamagnetic or paramagnetic shifts, hyperfine anomalies or other phenomena. The largest systematic uncertainty arises from the dependence of the field on the position in the magnet combined with the finite range straggling of the beam. This was estimated using positive muons by intentionally moving a graphite sample back and forth several cm along the beam direction, producing a frequency shift on the order of 20 ppm per cm at the point of steepest slope within the sample region. For dense samples, the muon stopping position could be controlled with confidence only to within about 1 cm, so the purely statistical uncertainties shown in Table XIV have been added

in quadrature with a systematic uncertainty of about 0.006 MHz to obtain the net uncertainties shown in Fig. 99.

Further work is required to convert our raw data into corrected magnetogyric ratios that can be critically compared with the predictions of theory. A thorough analysis of these corrections is beyond the scope of this Annual Report. We are therefore not in a position to make a definitive statement about the relativistic shift in $\mathrm{Cd}\mu^-$ where the disagreement between previous measurements is largest. However, such corrections would have to account for more than half the net shift in cadmium to bring it into agreement with the $(0.67 \pm 0.22)\%$ value claimed by Mamedov et al.

We invite others to make free use of the improved precision of our measurements.

Hyperfine transition in $^{23}\mathrm{Na}\mu^-$

When a negative muon reaches the $1s$ ground state of a muonic atom with a nucleus of non-zero spin, it experiences a strong hyperfine (HF) interaction with that nucleus; for heavier odd-A nuclei the effective HF magnetic field can be as high as 5×10^{10} T. This HF coupling makes the total spin $F^{\pm} = I \pm \frac{1}{2}$ an exceedingly good quantum number. If the muonic atom forms initially in the lower HF state (which will be the F^- state as long as the nuclear magnetic moment is positive), it will remain in that state and precess at the corresponding characteristic frequency ω_- in a transverse magnetic field until the muon decays or captures. The upper (F^+) state, however, is subject to radiative or (much more often) Auger transitions to the F^- state, which in heavy elements is $\sim$keV lower. (The radiative lifetime is much longer than that of the muon.) This Auger-mediated transition rate, R, was calculated for numerous nuclei by Winston, who also made the first direct measurement of $R_{\mathrm{F}} = 6.1 \pm 0.7 \ \mu\mathrm{s}^{-1}$ in muonic $^{19}\mathrm{F}$.

In lighter nuclei, especially those consisting of an odd proton outside a closed shell, the weak capture rate from one HF state is usually much faster than that from the other, reflecting the "$V - A$" character of the weak nuclear current. Precise measurements of these differences offer access to the induced pseudoscalar coupling constant at large q^2. In addition, they provide a superior method for direct determination of the HF transition rate R, since the rate of "neutrals" (photons and neutrons) from muon capture can actually increase with time if the slow-capturing HF state de-excites to the fast-capturing HF state. (The opposite situation will cause a neutrals rate that decreases more rapidly than the muon decays – which is also easy to interpret, but somehow seems less miraculous.) Such measurements thus inform us simultaneously of R and the differential capture rate.

If the F^+ and F^- capture rates are small or similar, or if R is very slow, it is often easier to measure R independently by observing the decay in time of the asymmetry of muon decay electrons in the F^+ state. As long as $R < \omega_+$ (the characteristic precession frequency of the F^+ state in a transverse magnetic field) it is easy to distinguish this asymmetry from that of the F^- state or various backgrounds; this "μ^-SR method" was used by Favart et al. in 1970 to measure R_{B} in muonic $^{10}\mathrm{B}$ and $^{11}\mathrm{B}$ and to set upper limits on R in muonic $^{6}\mathrm{Li}$, $^{7}\mathrm{Li}$ and $^{9}\mathrm{Be}$. That experiment established a new standard for μ^-SR measurements of R ($< 0.02 \ \mu\mathrm{s}^{-1}$ in muonic Li) and is unlikely to be much improved upon by that method, since spin relaxation by dipolar fields from neighbouring nuclei should have a rate $\sim 0.01 \ \mu\mathrm{s}^{-1}$. A more recent experiment by Wiaux et al. overcame that limitation by directly observing the 320 keV γ-ray from the excited state of $^{11}\mathrm{Be}$ created by nuclear muon capture on $^{11}\mathrm{B}$, an effect independent of dipolar relaxation. In this way they measured $R = 0.181 \pm 0.017 \ \mu\mathrm{s}^{-1}$ in muonic $^{11}\mathrm{B}$.

For $R > \omega_+$ it is sometimes feasible to measure R by a "residual polarization" method where the dephasing of the muon polarization (due to the exponential distribution of HF transition times) is measured as a function of magnetic field. This method was used to determine $R_{\mathrm{Al}} = 41 \pm 9 \ \mu\mathrm{s}^{-1}$ in muonic $^{27}\mathrm{Al}$, in embarassingly good agreement with Winston's prediction.

When $R \sim \omega_+$, one can use the μ^-SR method only if ω_+ is increased by applying a stronger magnetic field. For the HF transition rate of muonic $^{23}\mathrm{Na}$, where Winston predicted $R_{\mathrm{Na}} \approx 14 \ \mu\mathrm{s}^{-1}$, this requires a transverse magnetic field of ~ 1 T or higher, in which the radius of curvature of 60 MeV/c muons is ~ 2 m or less, causing deflection of the muon beam relative to its path in weak fields. As a result, the entire experiment must be designed and reconfigured for each target magnetic field, drastically reducing the versatility of the apparatus. This is one reason why no previous μ^-SR measurements have been made of R_{Na} in muonic $^{23}\mathrm{Na}$.

In 2002 we made a preliminary measurement in a magnetic field of 0.7 T where a precession signal from the F^+ HF state of muonic $^{23}\mathrm{Na}$ was just detectable for about one full period. That measurement gave a tentative value of $R_{\mathrm{Na}} = 13 \pm 4 \ \mu\mathrm{s}^{-1}$, consistent with Winston's prediction.

We have now made a more precise measurement in a transverse magnetic field of 2 T, using the newfound transverse polarization of M9B.

Combining this new value of R_{Na} with our previous preliminary measurement gives a best experimental estimate of $R_{\mathrm{Na}} = 13.7 \pm 2.2 \ \mu\mathrm{s}^{-1}$. This result is quite consistent with that measured by Gorringe et al. in

metallic sodium ($15.1 \pm 1.1\ \mu s^{-1}$) by observing characteristic γ-rays from ^{23}Ne (a product of μ^- nuclear capture), but less so with their previous result in NaF ($8.4 \pm 1.9\ \mu s^{-1}$), and even less with the measurements of Stocki *et al.* who found $R = 38 \pm 9\ \mu s^{-1}$ in Na metal and $R = 28 \pm 5\ \mu s^{-1}$ in NaH using the time dependence of capture neutrons. The latter three numbers disagree significantly with Winston's prediction of $R_{\mathrm{Na}} \approx 14\ \mu s^{-1}$.

It has been suggested that the HF transition rate may be altered by processes that depend on the chemical environment. One possibility would be delayed refilling of vacant electronic orbitals in insulating materials. A related medium-dependent mechanism might be external Auger.

The fitted frequencies of the F^+ and F^- states can be compared with the μ^+ frequency in aluminum at the same field, namely 271.5852 ± 0.0004 MHz. Correcting for a $+80 \pm 4$ ppm Knight shift in the latter gives a reference frequency of 271.5635 ± 0.0012 MHz. Comparing $\omega_\pm$ with this reference gives $\omega_+/\omega_\mu = 0.1878 \pm 0.0012$ and $\omega_-/\omega_\mu = -0.3534 \pm 0.0001$, in good agreement

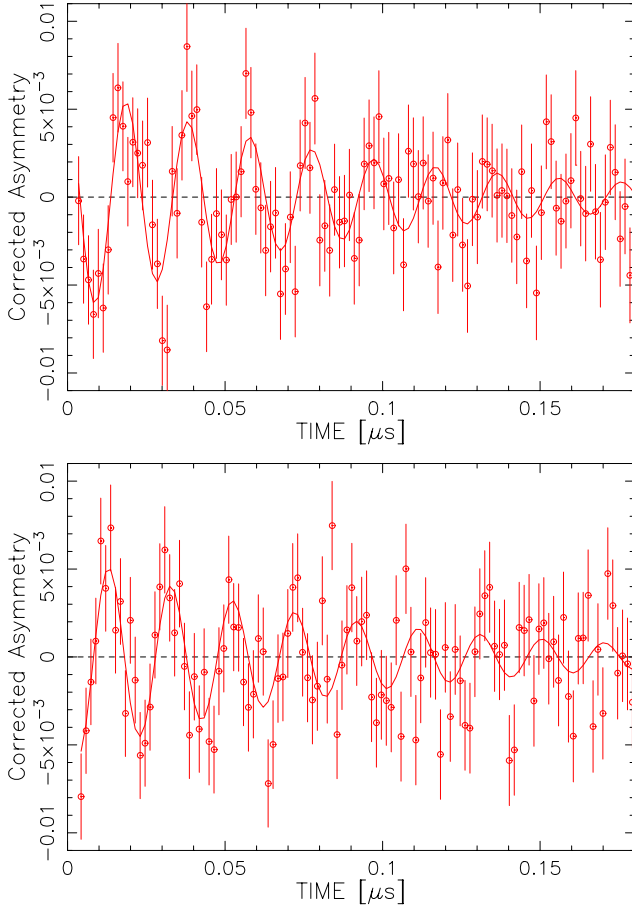with the frequencies predicted by simply combining the spins and magnetic moments of the muon and the nucleus, namely $\omega_+/\omega_\mu = 0.18765$ and $\omega_-/\omega_\mu = -0.35392$. The F^+ signal disappears within a few hundred ns but is visible in all four histograms; it is displayed in Fig. 100 with two histograms combined at a time to form the "real" (top) or "imaginary" (bottom) parts of the precession signal. This serves to reduce the statistical scatter for display purposes; the global fit to all four histograms simultaneously was used for the final results in Table XV.

Figure 101 shows the much smaller but longer-lived signal from the F^- state. For the figure, the complex asymmetry spectra were transformed into a reference frame rotating at a frequency slightly lower than ω_- and then packed to much coarser bins; this again serves to clearly display a signal that is otherwise (in the lab frame) invisible to the eye.

The signal amplitudes (muon decay asymmetries) can be compared with that of the positive muon in aluminum at the same field, $A_0 = 0.133 \pm 0.001$, to give the products of the residual μ^- polarizations $P_\pm$ and the fractional populations $f_\pm$ of the two HF states: $f_+ P_+ = A_+/A_0 = 0.0638 \pm 0.0083$ and $f_- P_- = A_-/A_0 = 0.0090 \pm 0.0015$. These numbers have not been corrected for the frequency dependence of the observed asymmetry; due to the finite time resolution of the detectors, higher frequency signals suffer an amplitude reduction. The reference asymmetry A_0 is therefore suppressed slightly, so that $f_+ P_+$ and $f_- P_-$ are slightly overestimated. For comparison, the asymmetry

Fig. 100. "Real" (top) and "imaginary" (bottom) parts of the precession signal of the F^+ hyperfine state in muonic ^{23}Na, showing the rapid decay into the F^- state.

Table XV. Results of fitting μ^-SR spectra in metallic sodium at 2 T. Only the physically relevant parameters are shown and only statistical uncertainties are given. Here τ_{Na} is the muon lifetime in muonic ^{23}Na, $A^\pm$ is the muon decay asymmetry in the $F^\pm$ HF state of muonic ^{23}Na, R is the $F^+ \to F^-$ HF transition rate, $\omega_\pm$ is the precession frequency of the $F^\pm$ state, $\phi_i^\pm$ is the apparent initial phase of the precession in the $F^\pm$ state and Λ is the spin relaxation rate of the F^- state, presumably caused by a combination of spatial inhomogeneity of the applied field, random fields from nearby magnetic moments and the effect of local electric field gradients on the ^{23}Na electric quadrupole moment. The asymmetric errors in R are returned by the MINOS command in MINUIT.

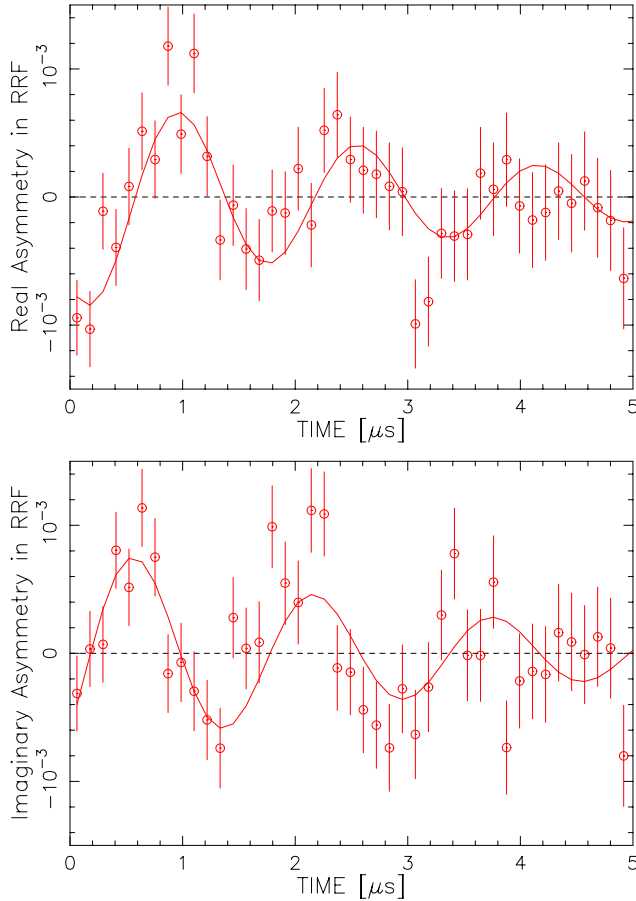|		
τ_{Na}	$=$	$(1.1955 \pm 0.0012) \times 10^{-6}$ s
A^+	$=$	0.00848 ± 0.0011
R	$=$	$\left(13.97^{+2.9}_{-2.4}\right) \times 10^6$ s^{-1}
ω_+	$=$	$2\pi \times (51.0 \pm 0.3$ MHz$)$
ϕ_+	$=$	$-18.6° \pm 11°$
A^-	$=$	0.0012 ± 0.0002
Λ	$=$	$(0.024 \pm 0.1) \times 10^6$ s^{-1}
ω_-	$=$	$2\pi \times (-95.9676 \pm 0.015$ MHz$)$
ϕ_-	$=$	$-175.4° \pm 13.4°$

Fig. 101. Precession signal of the F^- hyperfine state in muonic ^{23}Na, viewed in the rotating reference frame at exactly $\Omega_{\mathrm{RRF}} = -95.3$ MHz. The apparent frequency of -0.6676 ± 0.015 MHz is added to Ω_{RRF} to obtain the result shown in Table XV.

in muonic carbon (graphite) at the same field, $A_{\mathrm{C}} = 0.0256 \pm 0.0008$, gives $P_{\mathrm{C}} = A_{\mathrm{C}}/A_0 = 0.1925 \pm 0.0062$, generally regarded as one of the highest residual μ^- polarizations available.

In muonic atoms, negative muons lose polarization due to $\vec{L} \cdot \vec{S}$ couplings in atomic transitions down to the ground state; in the case of nuclei with spin, this is complicated by the HF structure of the atomic levels, which can also lead to partial polarization of the nuclei themselves. This makes the populations and polarizations of the final $F^\pm$ states difficult to predict. If we were to assume the same initial polarization for both states, $P_+ = P_-$, then we could conclude that $(87.6 \pm 11.4)\%$ of muonic ^{23}Na atoms are initially in the F^+ state and $(12.4 \pm 2.1)\%$ are initially in the F^- state. Such experimental values should be useful for an unambiguous interpretation of muon capture results in terms of the effective weak couplings $\tilde{g}_a$ and $\tilde{g}_p$.

Experiment 938
Muonium formation and ionization in semiconductors and insulators
(V.G. Storchak, Kurchatov Inst.; J.H. Brewer, UBC/TRIUMF)

To date, most muonium studies in semiconductors have been focused on the lowest electronic states without considering the details of how these states are formed: spectroscopic experiments have revealed two quite different types of Mu centres. These centres are characterized by their different muon-electron hyperfine interactions. So-called "normal" muonium has an isotropic hyperfine interaction with a hyperfine frequency A about half of that in the free Mu atom ($A_0 = 4463$ MHz) and is located at the tetrahedral interstitial site; it is therefore denoted $\mathrm{Mu}_{\mathrm{T}}^0$. "Bond-centred" muonium, with a small anisotropic hyperfine interaction ($A \sim A_0/50$) because of somewhat extended electron distribution, is located near the centre of the relaxed crystal bond and is thus denoted $\mathrm{Mu}_{\mathrm{BC}}^0$. Both centres are associated with quite deep energy levels in the gap.

Experiments in electric fields designed for detailed studies of muonium formation processes in semiconductors have revealed an essential difference between $\mathrm{Mu}_{\mathrm{BC}}^0$ and $\mathrm{Mu}_{\mathrm{T}}^0$: while the former is found to form via the electron capturing initially into a very excited state and then cascading down through the weakly bound (shallow) short-lived hydrogenic effective-mass state (EMS) into a deep ground state, the latter is believed to form directly into a deep state.

No matter how the muonium atom is formed, it may act as a trapping centre or a recombination centre depending on the host material and the temperature range in the same manner as other impurities in a semiconductor. Indeed, Mu (or a filled trap) is typically found at lower temperatures, while a diamagnetic state (which could be an ionized trap or, alternatively, a recombination centre) is observed at higher temperatures. This "general trend" of muonium spectroscopy (high probability of Mu formation at low temperatures along with the absence of muonium at high temperatures) has so far been explained as Mu ionization at elevated temperatures: the muonium atom loses its electron into the conduction band in an activated Arrhenius-like mechanism – a process which suggests that the Mu atom is a trapping centre. Although it is easy to understand such muonium ionization for a shallow Mu centre (either for a long-lived state or a short-lived one), thermal ionization of a deep-level Mu state encounters certain difficulties. Indeed, the binding energy of a shallow Mu state typically amounts to about 10 meV, which is less than the typical Debye energy (several tens of meV), while the typical binding energy

of a deep Mu state significantly exceeds the Debye energy. Under these circumstances, Mu ionization via an activated Arrhenius-like mechanism requires simultaneous absorbtion of many phonons – a process which is severely suppressed. These features of Mu formation and ionization processes make it hard to consider certain shallow (and the majority of deep) muonium centres as trapping centres.

Deep muonium state in InSb: recombination centre vs. trapping centre

To date, various muonium centres in semiconductors (as well as in the above discussion) have been considered to have their energy levels (either deep or shallow, lying below the conduction band minima either a few tenths or a few hundredths of an eV, respectively) in the forbidden gap. In this case certain Mu centres may be treated as trapping centres. Another situation is realized in narrow-gap semiconductors where deep Mu energy level cannot be accommodated in the gap.

Here we present new results on the deep-level muonium centre in InSb – a semiconductor with an extremely narrow energy gap. We argue that this centre can be better considered as a recombination centre rather than a trapping centre.

Last year our experiments in high magnetic field in both n- and p-type InSb revealed several signals which were identified as those corresponding to a paramagnetic muonium state and diamagnetic state (probably a bare muon). In last year's Annual Report we showed the magnetic field dependence of muonium precession frequencies ν_{12} and ν_{34} which correspond to muon spin flipping in states with electron spin "down" and "up", respectively, along with the diamagnetic

frequency (Fig. 102). Fitting to a Breit-Rabi Hamiltonian showed that such field dependence of the precession frequencies corresponded to a muonium centre with an isotropic hyperfine interaction $A = 2464(1)$ MHz.

This value for the hyperfine interaction parameter A is characteristic of tetrahedral muonium centre Mu_T^0 observed in other III-V semiconductors GaAs and GaP as well as in elemental group-IV semiconductors Si, Ge and C. The high value of A is taken as evidence for a highly localized Mu centre in InSb; the characteristic radius is expected to be on the order of the Bohr radius. In accordance, the energy level of such centre is expected to lie quite deep below the conduction band minimum, a rough estimate being about 1 eV. Such a high value for the binding energy of a Mu centre does not allow one to accommodate this energy level in the extremely narrow forbidden gap of InSb (0.24 eV at 80 K). No matter how weird it looks, we probably have to admit that this Mu energy level lies in the valence band. It is worth noting that several theoretical attempts to account for the observed high value for the hyperfine frequency A of Mu_T^0 in semiconductors have come to the same conclusion.

No matter where one can accommodate the energy level for such a deep Mu state in a semiconductor (in the forbidden gap or in the valence band), the high value of its binding energy ensures that the ionization of this state is expected to occur only at very high temperature. In contrast to all other deep Mu centres in semiconductors, experiments in InSb show that Mu centre starts to disappear at about 20 K. Figure 103 presents temperature dependence of the relaxation rate of Mu signals in magnetic field 3 T. Above about 60 K we found no Mu signal at all.

Fitting this temperature dependence with an Arrhenius law yields $E_a = 75(15)$ K for the activation
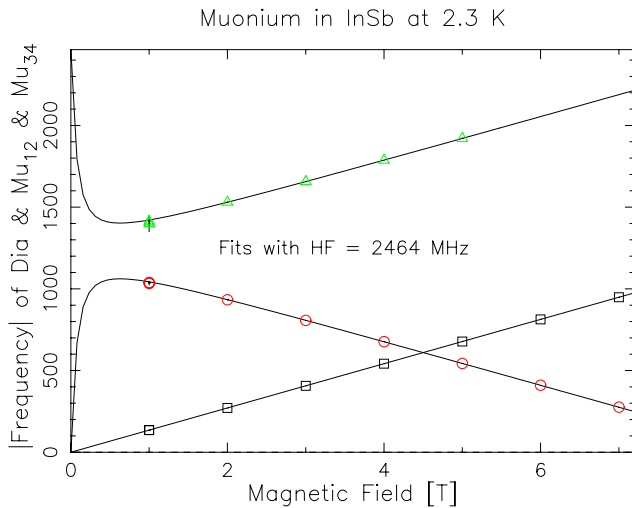

Fig. 102. Magnetic field dependences of two Mu frequencies (ν_{12}: circles and ν_{34}: triangles) and the diamagnetic frequency (squares) in n-type (10^{12} cm^{-3}) InSb. Solid lines for Mu frequencies present fit according to isotropic muonium hyperfine interaction.
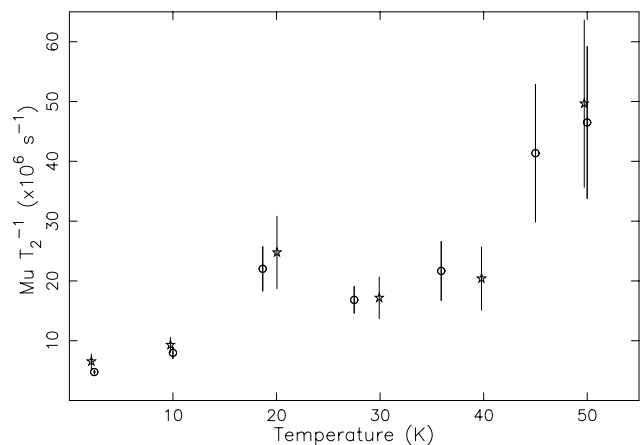

Fig. 103. Temperature dependence of the exponential spin relaxation rate of the Mu signal in n-InSb (circles) and p-InSb (stars) in a transverse magnetic field of 3 T.

energy. Neither this activation energy nor the temperature range of Mu disappearance in InSb are consistent with thermal ionization of a deep Mu centre. Both the activation energy and the temperature range, on the other hand, might indicate that this centre is formed via initial electron capture into very excited orbit – a process analogous to $\mathrm{Mu}^0_{\mathrm{BC}}$ formation in GaAs and GaP. Then thermal ionization of Mu might take place from an intermediate weakly bound highly excited state. The key to distinguishing this scenario from prompt muonium formation is an application of electric field. Unfortunately, our InSb samples do not hold even very weak electric field (probably due to activation of very shallow impurity centres). However, we argue that the possibility of electron capture into (and thus thermal ionization from) some weakly bound excited state of the observed Mu centre in InSb can be ruled out: we found no electron freezeout effect – a characteristic signature of an intermediate weakly bound Mu state.

We further argue that the observed disappearance of Mu signals at low temperatures may be consistent with recombination of the Mu electron with thermally activated holes in InSb: the binding energy of shallow acceptors in InSb amounts to about 100 K. This process, however, requires absorbtion of energy in the eV range, which is much higher than the Debye energy. Therefore neither acoustic nor optical phonons can be effective here. Then the only energy bath which can deposit this energy for hole capture by the Mu atom is the electron subsystem. We suggest that processes analogous to impact ionization may be responsible for the disappearance of the Mu centre at low temperatures in InSb. Such electron-hole recombination is commonly observed for deep-level defects in semiconductors.

Experiment 942
Magnetic fluctuations near metal insulator transitions in ruthenate pyrochlores
(S.R. Dunsiger, McMaster; R.F. Kiefl, UBC)

The nearly free electron model may often successfully describe the band structure of a crystal, the highest band being completely filled for insulators or only partially so for metals. However, many transition metal oxides with partially filled d-electron bands have nonetheless been found to be poor conductors or indeed insulators. The origin of this behaviour is thought to be the Coulomb repulsion between electrons: strong electron-electron correlations. Indeed, an otherwise insulating material may be driven into a metallic state in a controllable way with doping, chemical composition, pressure or magnetic field. Such metal-insulator transitions are widely observed in condensed matter physics. The scientific interest in these materials is based on the fact that near the transition point the metal shows fluctuations of spin, charge and orbital degrees of freedom.

The focus of Expt. 942 is the study of pyrochlores with chemical composition $A_2B_2O_7$ where only the B site is occupied by a magnetic ion, in particular $Y_{2-x}Bi_xRu_2O_7$. This system may be driven in a controlled manner from a geometrically frustrated insulator to a Pauli paramagnetic metal with increasing Bi doping. Susceptibility measurements on insulating $Y_2Ru_2O_7$ by Yoshii and Sato [J. Phys. Soc. Jpn. **68**, 3034 (1999)] show evidence of an ordering transition at $T_G \sim 76$ K. Doping with Bi on the Y site increases the lattice constant and the system becomes progressively more metallic as the Bi 6p states mix with 4d states of Ru via the framework oxygen [Cox *et al.*, J. Solid State Chem. **62**, 360 (1986)]. There is a metal-insulator transition at $x = 0.9$. The ordering transition temperature is also progressively suppressed and broadened. From published work [Yoshii and Sato *op. cit.*], T_G is expected to go to zero in $Y_1Bi_1Ru_2O_7$. It is important to note that, while this Mott-Hubbard system is tuned through a bandwidth controlled metal-insulator transition, the concentration of magnetic Ru ions is not altered. In other words, the magnetic sublattice has not been diluted.

Muon spin relaxation is one of the principal methods we have used to characterize the dynamic behaviour, since it is uniquely sensitive to the low frequency magnetic fluctuations which are often present in these systems. Longitudinal field measurements have provided insight into the ordering transition in this family of compounds. Alternatively, in a tranverse field configuration, measurements of the muon spin precession frequency with respect to the applied field probe the contact hyperfine and dipolar fields within these materials and yield information on the local spin susceptibility. Anomalous behaviour has been observed in $(V_{1-x}Cr_x)_2O_3$, the archetypal system undergoing a bandwidth controlled metal-insulator transition [Gossard *et al.*, Phys. Rev. **B3**, 3993 (1991)], where the frequency shift as measured with NMR does not track the bulk susceptibility χ. We have therefore recently undertaken a series of studies of the shift in the muon spin precession frequency as a function of temperature in $Y_{2-x}Bi_xRu_2O_7$ to compare the local and bulk susceptibilities.

Transverse field muon spin rotation measurements on sintered powder samples were carried out on the M15 beam line at TRIUMF, using the Belle magnet with high timing insert. The frequency shift measures the real part of the dynamic susceptibility χ', while the linewidth may be related to the imaginary part χ'' through the fluctuation-dissipation theorem. The frequency shift is then given by $(\nu_{\mathrm{Sample}} - \nu_{\mathrm{CaCO_3}})/\nu_{\mathrm{CaCO_3}}$. Calcium carbonate is used as a refer-

ence material as it induces only negligibly small chemical shifts in the muon spin precession frequency. The temperature variation of the paramagnetic frequency shifts in an applied magnetic field of 40 kOe is shown in Fig. 104 for four Bi concentrations ($x = 0$, 0.9, 1.0, 2.0). Note that a negative frequency shift is observed. Naively one might expect a positive shift in a paramagnetic material. However, in general, in an isotropic system of point magnetic dipoles and assuming axial symmetry, the frequency shift in a polycrystalline paramagnet is solely a measure of the local contact hyperfine field at the muon site, since the dipolar field contributes nothing in an isotropic powder material [Ibers *et al.*, Phys. Rev. **121**, 1620 (1961)]. The sign of the hyperfine coupling may take either positive or negative values. More generally, dipolar fields will also typically contribute, given an anisotropic g tensor.

The measurements of the paramagnetic frequency shifts may be compared with those of the bulk susceptibility, shown in Fig. 105. These data were also collected by field cooling (FC) the samples in an applied magnetic field of 40 kOe. The magnetic history of the samples during the bulk and local probe measurements is thus equivalent. There are several features of interest. As may be seen in Fig. 105, the bulk susceptibility decreases with increasing Bi concentration, despite the fact that the magnetic Ru^{4+} ion concentration has not been altered. Rather, the size of the permanent magnetic moment of the Ru ion is decreasing as the valence electrons become more itinerant in character. Surprisingly, the paramagnetic frequency shifts do not show this same monotonic trend. The magnitude of the shift in $Y_2Ru_2O_7$ is anomalously small. This is unlikely due to an instrumental effect, since the data shown are a combination of two sets taken approximately one week
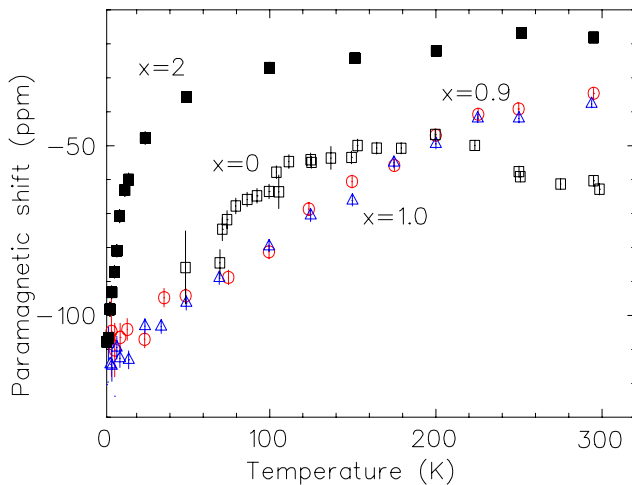

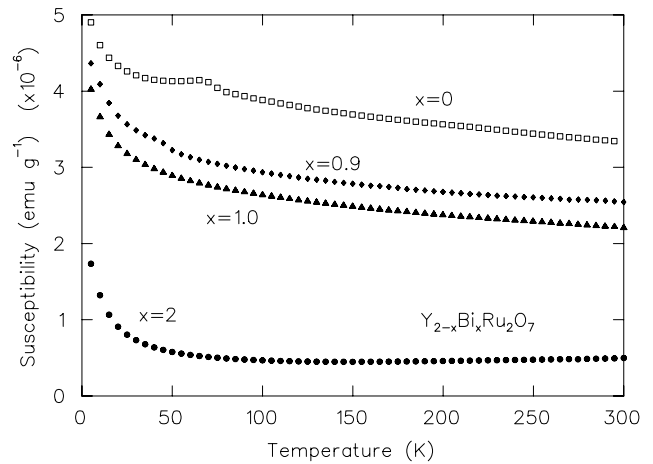Fig. 104. Temperature dependence of the paramagnetic frequency shift in $Y_{2-x}Bi_xRu_2O_7$ in an applied transverse magnetic field of 40 kOe.

Fig. 105. Temperature dependence of the bulk susceptibility in $Y_{2-x}Bi_xRu_2O_7$ in an applied magnetic field of 40 kOe.

apart, the remaining samples being studied in the intervening period.

Another interesting anomaly is observed in $Y_2Ru_2O_7$: the paramagnetic frequency shift undergoes a change in the slope of its temperature dependence. Initially increasing with temperature, the frequency shift starts to decrease again above 200 K. No such effect is observed in measurements of the bulk susceptibility, which decreases monotonically with increasing temperature. This disparity could arise either because of a muon induced effect or temperature dependence in the contact hyperfine and/or dipolar field. One might anticipate such a change in the local field in the neighbourhood of the metal-insulator transition, by analogy with $(V_{1-x}Cr_x)_2O_3$. However, its origin in pure $Y_2Ru_2O_7$ is still under investigation.

Finally, the low temperature upturn in both the bulk susceptibility as well as the magnitude of the frequency shift of all four samples is likely due to paramagnetic impurities.

Currently, we are working to quantify the various contributions to the bulk and local susceptibilities. We would like to compare these results with our existing data on $Y_2Mo_2O_7$. The latter compound is an isostructural geometrically frustrated 4d electron system. A comparison of the two could thus provide insight into the role of the 4d magnetic species on the metal-insulator transition.

Experiment 944
Muonium in silicon carbide
(R.L. Lichti, Texas Tech; K.H. Chow, Alberta)

The goal of Expt. 944 has been to investigate the muonium states formed in the three most common structures of SiC, the cubic 3C and the 4H and 6H hexagonal polytypes. We initially focused on the Mu^0

signals observed in the 4H and 6H structures, examining n-type, p-type and high-resistivity samples of each.

Following the initial hyperfine spectroscopy using the HiTime spectrometer, we tentatively identified likely sites for the observed Mu^0 states [Lichti *et al.*, Phys Rev **B70**, 165204 (2004)]. Figure 106 shows a section of the 4H structure with various theoretically predicted sites marked and labelled. Based on the latest predictions and the acceptor behaviour we observe for one of the paramagnetic signals in 4H-SiC, hyperfine values ranging from 3010 to 3030 MHz extrapolated to zero temperature have been assigned to a T_{Si} site which is predicted to be the stable locations for both Mu^0 and Mu^- in 4H-SiC. There are two slightly inequivalent T_{Si} sites in the 6H structure, leading to two signals in this range in the high-resistivity 6H-SiC samples. We have also assigned HF values below 2900 MHz to the AB_{Si} locations near the centre of the 2H-like channels for one signal in each of the 4H and 6H structures. Additionally, a second signal in this region seen only at very low temperatures in n-type 6H-SiC is suggested to be formed via electron capture by a Mu^+ at its predicted stable site, AB_C, which should then quite easily switch to T_{Si} at relatively low temperatures.

In the most recent beam time we investigated the dynamics reported earlier for 6H samples. In the high resistivity 6H sample, high frequency spin precession data imply a large dip in amplitude for all of the Mu^0 signals near 150 K and a peak in the associated relaxation rates. Longitudinal relaxation rates also show a peak near 170 K and a second one near 280 K in n-type 6H, as reported previously. Figure 107 shows the

Fig. 107. The composite Mu^0 relaxation rates (top), and the amplitudes for the diamagnetic (open squares) and triplet Mu^0 signals (filled squares) (bottom), in TF-μSR data for high-resistivity 6H-SiC taken at 15 G.

amplitudes and Mu^0 relaxation rate for low-field data taken to explore the composite Mu^0 dynamics above 300 K. These data suggest at least partial ionization of Mu^0 states above room temperature as suggested from the high-frequency results, but do not distinguish which Mu^0 state is involved (all three showed an increase in relaxation rate on approach to 300 K in the HiTime data). We plan to investigate this region further with rf or microwave driven resonance experiments in the near future in order to separate the dynamics arising from each neutral muonium centre.

Experiment 945
Muoniated radicals formed from carbenes and carbene analogues
(P.W. Percival, SFU)

Experiment 945 has its origins in Expt. 883, which concerns muoniated methyl and its derivatives. One method for creating such α-muoniated radicals involves addition of Mu to carbenes (see Fig. 108a). Carbenes
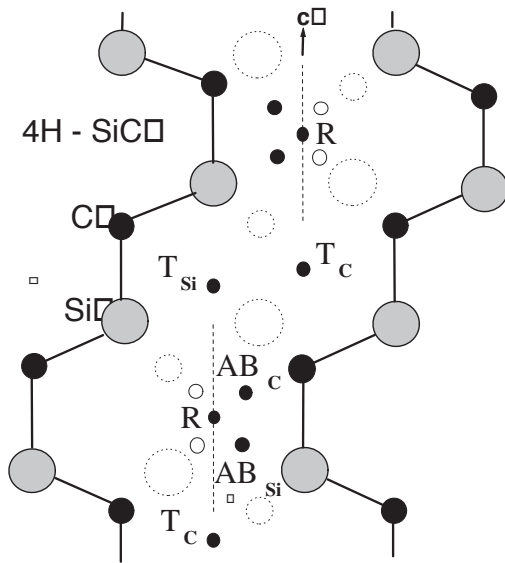

Fig. 106. Possible sites for Mu in the 4H structure of SiC. 6H-SiC will have an additional step in the zig-zag channel and a second type of T_{Si} site, but is otherwise similar.
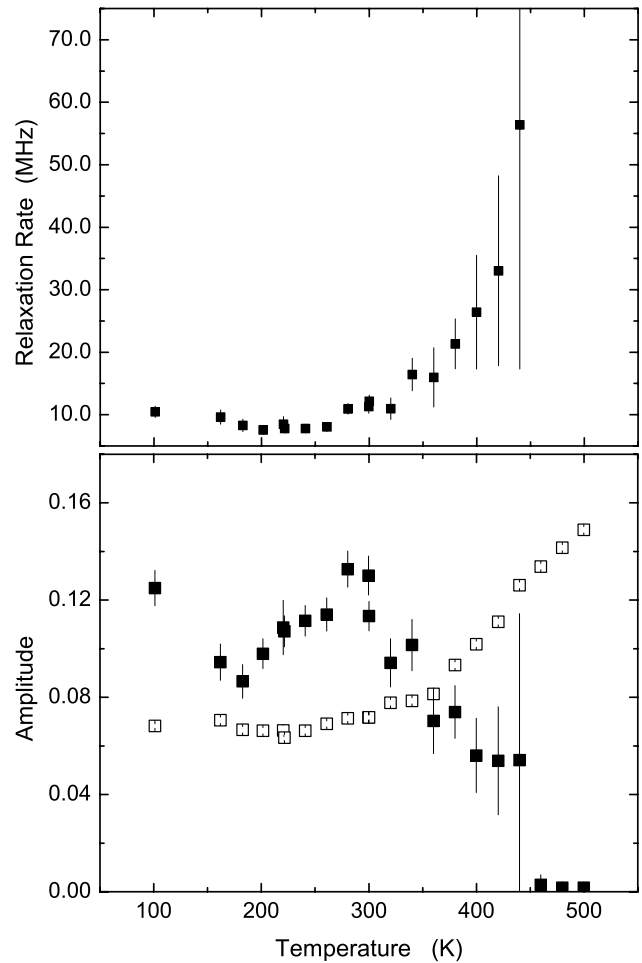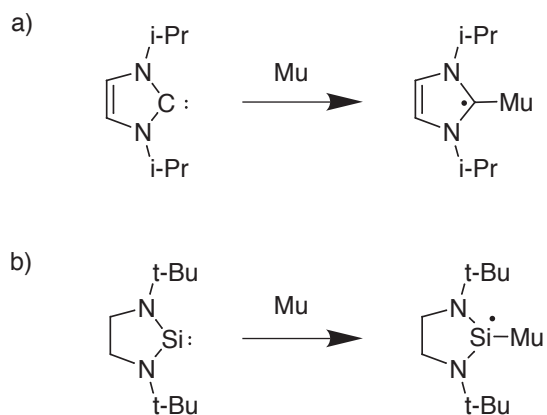
Fig. 108. (a) Muonium adds to a carbene to form a sub-stituted methyl radical. (b) Muonium adds to a silylene to form a silyl radical.

$(R_2C:)$ are molecules that possess a neutral dicoordinate carbon atom with six valence electrons, which generally results in high reactivity, so that carbenes tend to be considered only as reaction intermediates. However, over the past decade several singlet carbenes have been synthesized and isolated. The addition of a hydrogen atom to a dicoordinate carbon corresponds to a very significant chemical process – the isolated creation of a new chemical bond – and Expt. 945 was conceived to explore this fundamental chemistry.

A preliminary account of our experiments with carbenes was included under Expt. 883 in the 2002 TRI-UMF Annual Report; full details have since been published [McKenzie et al., J. Am. Chem. Soc. **125**, 11565 (2003); McKenzie, Ph.D. thesis, SFU (2004)]. A new aspect of Expt. 945 is the extension of this novel chemistry to analogous molecules containing other Group 14 elements at the carbene site, such as the silylene depicted in Fig. 108b. Stable molecules containing a divalent silicon atom were synthesized for the first time only a few years ago. Nevertheless, they have been hypothesized as intermediates in many thermal and photochemical reactions of organosilicon compounds, so questions concerning their reactivity are of considerable import. When Expt. 945 was first proposed there was no literature at all on radical reactions of stable silylenes. However, a short communication has since appeared reporting the first ESR spectra of radical adducts of a silylene [Tumanskii et al., J. Am. Chem. Soc. **126**, 7786 (2004)]. Relatively large radicals were chosen so that the silyl radical products are stabilized by electron delocalization. Our own experiments complement this work since we employ Mu as an isotopic substitute for H. Instead of creating a carbon-silicon bond at the reaction site, we form a silicon-hydrogen bond. The resulting radicals are short-lived and much closer to the intermediates posited in industrial processes.
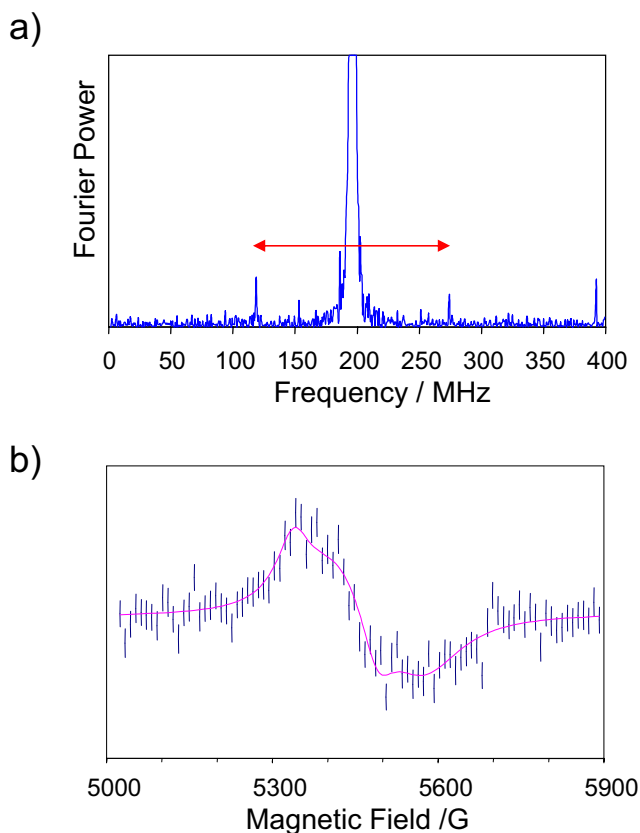

Fig. 109. (a) TF-μSR and (b) μLCR spectrum of the silyl radical formed from the reaction of muonium with a stable silylene.

To date we have been successful in detecting one muoniated silyl radical; the transverse-field μSR and level-crossing spectra are shown in Fig. 109.

The second theme pursued in Expt. 945 during 2004 concerns an investigation of muonium addition to azulene (Fig. 110). Azulene, $C_{10}H_8$, is a polycyclic
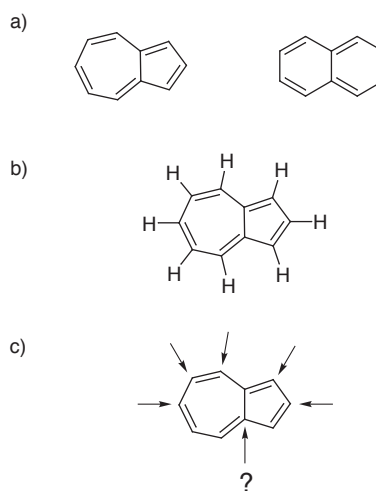

Fig. 110. (a) Azulene is an isomer of naphthalene. (b) The bridgehead carbons do not have attached H atoms. (c) Five of the six chemically distinct carbon sites are expected to be more reactive than the bridgeheads.

aromatic hydrocarbon consisting of fused 5- and 7-membered rings. It is an isomer of naphthalene, to which it rearranges at high temperature. A recent computational study [Alder *et al.*, J. Am. Chem. Soc. **125**, 5375 (2003)] suggests that the mechanism for this reaction involves bond formation at a bridgehead carbon, i.e. at a carbon shared by the two rings. Our own experience (Expt. 749) led us to doubt this hypothesis, so we decided to investigate the reactivity of azulene towards H atom attack by identifying the radical products formed by Mu addition.

Preliminary calculations suggested preferential addition at two sites on the 5-ring. However, μSR experiments soon showed the situation to be more complicated. It is evident from Fig. 111 that there are *at least* five distinct radical products, each characterized by a pair of precession frequencies. Since this is a power spectrum, the amplitudes are proportional to the yields squared. Thus, the five strongest pairs of lines represent radicals with relative yields of approximately 1:2:2:2:2. Our previous work with pyrene and fluoranthene [Brodovitch *et al.*, Can. J. Chem. **77**, 326 (1999); *ibid.* **81**, 1 (2003)] clearly showed a preference for carbon sites bearing a hydrogen, suggesting that the radical signals in Fig. 111 are the products of Mu addition to the sites indicated by the arrows in Fig. 110c. These have degeneracies 1:2:2:2:1. The deviation of the experimental yields from these ratios could be explained by differential reactivity of the sites, but there is also the possibility that Mu does indeed add to one of the bridgehead carbons.

To resolve this question we need to assign molecular structures to each of the radical signals. This can be done by calculating the structures and properties of the radical isomers. The calculated muon hyperfine constants can be compared with values derived from the μSR spectrum, and the associated proton hyperfine constants can then be used to predict resonance positions in the μLCR spectrum. However, this is not trivial, since the spectrum obviously contains many signals (see Fig. 112). Detailed analysis is under way.

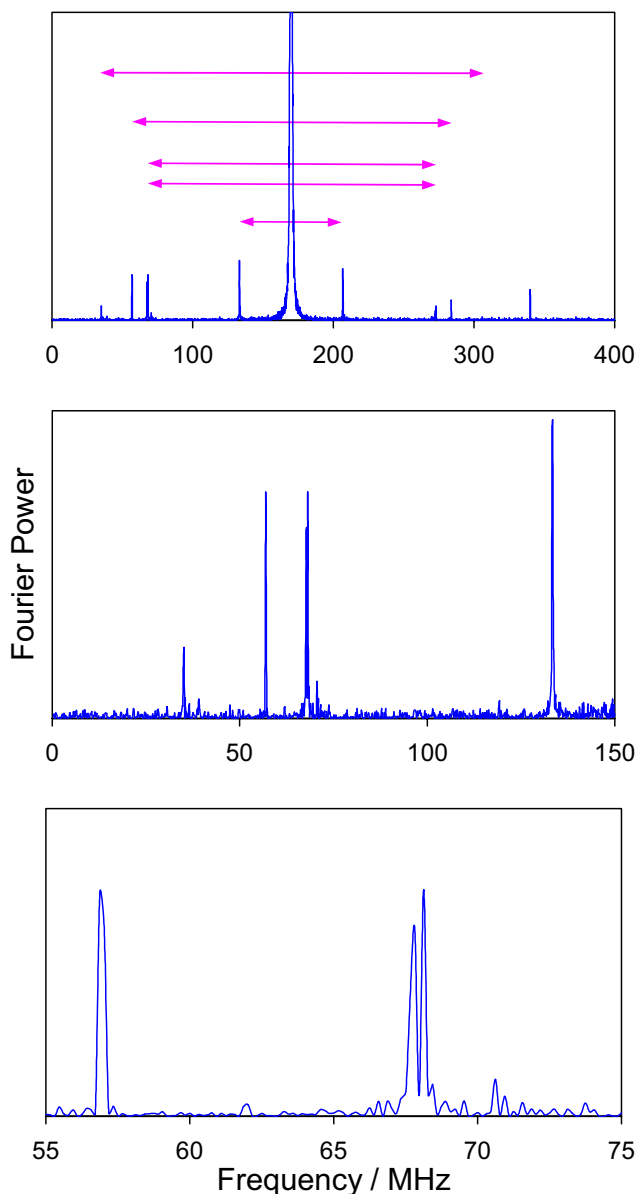Fig. 111. TF-μSR spectrum obtained from a solution of azulene in tetrahydrofuran. Each muoniated radical gives rise to a pair of precession frequencies, as indicated in the top panel.
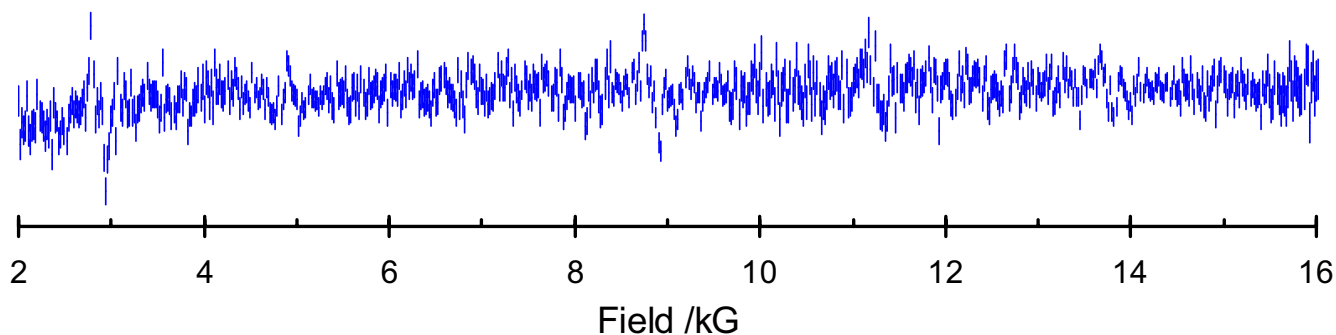

Fig. 112. A synthesis of μLCR spectra obtained from a solution of azulene in tetrahydrofuran.

Experiment 949

μSR study of magnetic order in high-T_c superconductors under high pressure

(J. Arai, T. Goko, Tokyo U. Science)

Anomalous suppression of superconducting transition temperature T_c observed in a narrow range of $x \sim 1/8$ for $La_{2-x}M_xCuO_4$ (M = Ba, Sr), which is called the "1/8 problem", is one of the most important issues to understand the relation between superconductivity and magnetism in high-T_c cuprates. At the beginning, the 1/8 problem was considered to be particular to La-214 compounds. However, 1/8 anomaly is also observed in Bi-2212 and Y-123, suggesting that the 1/8 problem is a common property of high-T_c superconductors.

Structural instability is inherent in La-214 compounds, which are the most typical system in high-T_c superconductors. The crystal structure is closely related to the electronic state in this system. With decreasing temperature, La-214 compounds undergo a well-known phase transition from a high-temperature tetragonal (HTT) structure to a low-temperature orthorhombic (LTO) structure except for the overdoped region. In addition, $La_{2-x}Ba_xCuO_4$ (LBCO) displays a second transition to a low-temperature tetragonal (LTT) structure around $x = 1/8$ at low temperatures. Because superconductivity is strongly suppressed in LBCO around $x = 0.125$ and slightly suppressed in $La_{2-x}Sr_xCuO_4$ (LSCO) around $x = 0.115$, it is widely believed that the LTT structure plays an important role in suppressing superconductivity around $x \sim 1/8$.

On the other hand, in La-214 compounds around $x \sim 1/8$, magnetic order has been observed by neutron scattering experiments and μSR experiments. These results indicate the close relation between the suppression of superconductivity and the appearance of magnetic order.

In order to clarify the relation among superconductivity, the magnetic order and the LTT structure, we have performed the zero-field μSR measurement and the resistivity measurement in LBCO with $x = 0.125$ and 0.135 under high pressure up to $\sim$1.5 GPa by using a pressure cell which we have developed. The LTT phase of LBCO with $x = 0.125$ is suppressed by applying pressure up to $\sim$0.6 GPa [Katano *et al.*, Phys. Rev. **B48** (1993)]. In La-214 compounds, the carrier concentration hardly depends on pressure [Tanahashi *et al.*, Jpn. J. Appl. Phys. **28** (1989)] in contrast to other high-T_c cuprates. We can control the LTT structure by applying pressure without changing the carrier concentration.

Figures 113 and 114 show the μSR spectra for LBCO with $x = 0.125$ at $P \sim 0.5$ GPa and 1.5 GPa, respectively. The LTT structure spreads over the
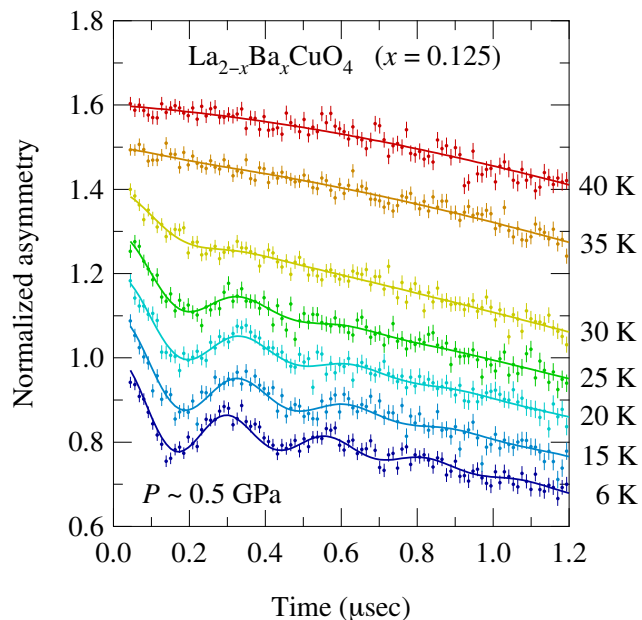

Fig. 113. ZF-μSR spectra of LBCO with $x = 0.125$ at $P \sim 0.5$ GPa. The spectra are vertically offset for clarity.
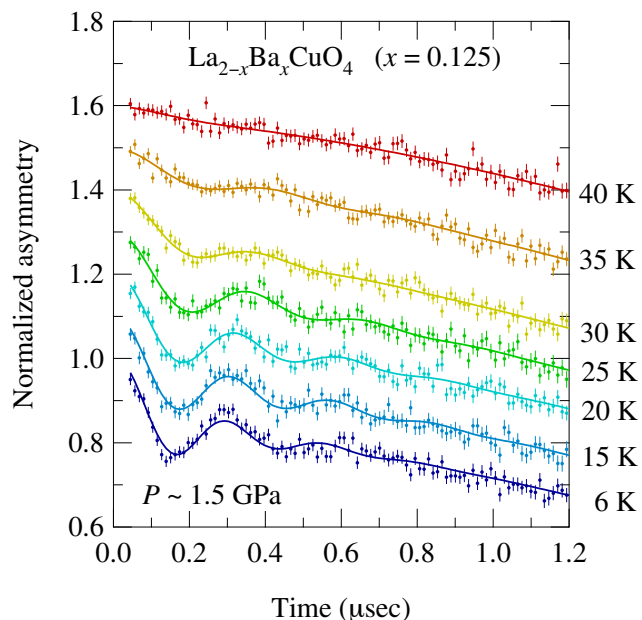

Fig. 114. ZF-μSR spectra of LBCO with $x = 0.125$ at $P \sim 1.5$ GPa. The spectra are vertically offset for clarity.

sample at $\sim$0.5 GPa and vanishes at $\sim$1.5 GPa. An oscillation component is observed at low temperatures under both pressures. Since the oscillation component indicates the magnetic order, this result suggests that the LTT structure is dispensable for the appearance of the magnetic order. These spectra include contributions from the sample and the pressure cell. The ratio of the sample signal to the background is typically 1 : 2. The slow relaxation observed over a wide temperature range is due to the pressure cell. Here we define the magnetic ordering temperature T_m as the temperature

where an oscillation component starts to appear in the μSR spectra. For example, in the case of $P \sim 1.5$ GPa, T_m exists between 35 and 40 K.

The values of T_c and T_m for LBCO with $x = 0.125$ are plotted as a function of pressure in Fig. 115. Here T_c is determined by zero resistivity. With increasing pressure, T_c increases linearly with an initial rate of $dT_c/dP \sim +8.1$ K/GPa. At $P_d \sim 1.1$ GPa, dT_c/dP changes to $+1.9$ K/GPa. It seems that P_d corresponds to the LTT-LTO phase transition pressure, since dT_c/dP is affected by the crystal structure in La-214 compounds, and dT_c/dP observed in the orthorhombic phase of LSCO is $\sim +2$ K/GPa. On the other hand, T_m does not decrease but increases, suggesting that the suppression of T_c has no correlation with T_m in LBCO with $x = 1/8$.

Figures 116 and 117 show the μSR spectra for LBCO with $x = 0.135$ at ambient pressure and at $P \sim 1.1$ GPa, respectivly. The LTT structure spreads over the sample at ambient pressure and vanishes at $P \sim 1.1$ GPa. An oscillation component is observed at low temperatures under both pressures, suggesting that the LTT structure is dispensable for the appearance of the magnetic order also in LBCO with $x = 0.135$. The ratio of the sample signal to the background is typically $1:4$, because of failure in tuning of muon momentum. The magnetic volume fraction estimated from the amplitude of the oscillation component in the μSR spectra is reduced from $\sim 100\%$ to $\sim 30\%$ by applying pressure up to 1.1 GPa.
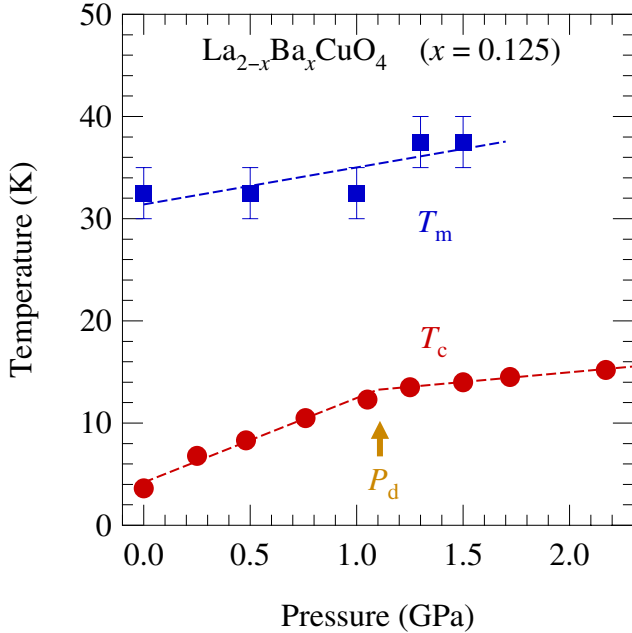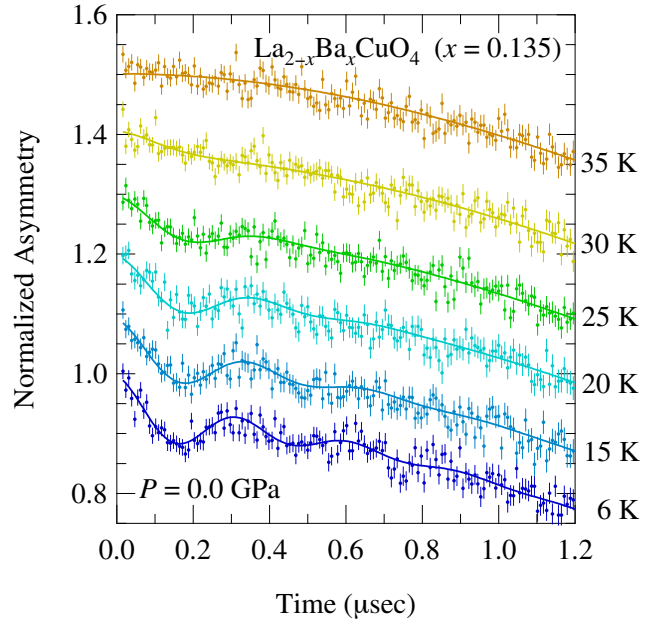

Fig. 116. ZF-μSR spectra of LBCO with $x = 0.135$ at ambient pressure. The spectra are vertically offset for clarity.
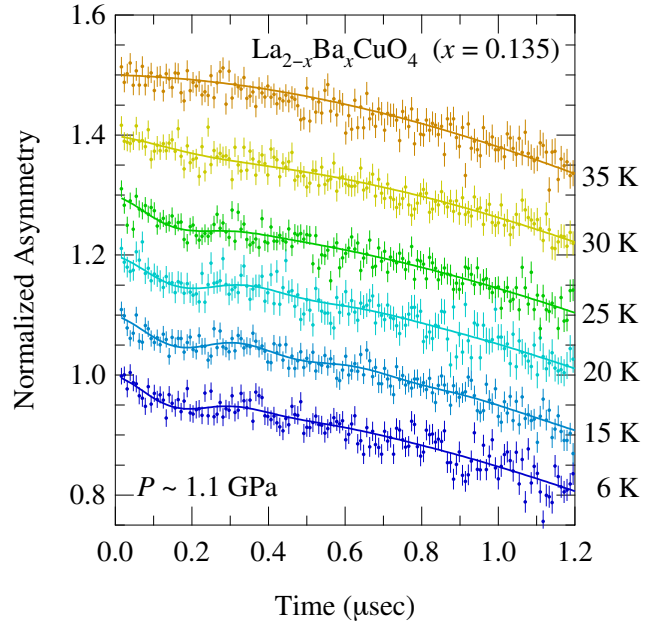

Fig. 117. ZF-μSR spectra of LBCO with $x = 0.135$ at $P \sim 1.1$ GPa. The spectra are vertically offset for clarity.

For LBCO with $x = 0.135$, T_c drastically increases with increasing pressure, as shown in Fig. 118. At $P_d \sim 1.0$ GPa, T_c reaches ~ 30 K and dT_c/dP changes to $+2.1$ K/GPa which corresponds to the pressure dependence of T_c in the orthorhombic phase. On the other hand, T_m hardly changes. The suppression of T_c therefore has no correlation with T_m. We speculate that the suppression of T_c is closely related to the magnetic volume fraction.
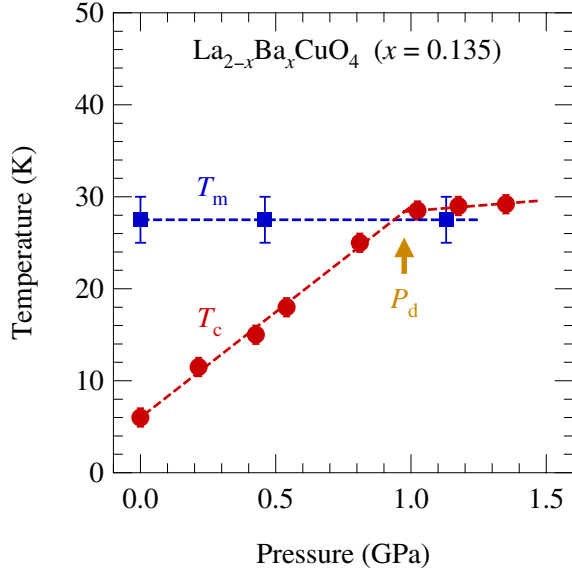

Fig. 115. Pressure dependence of T_m and T_c for LBCO with $x = 0.125$. P_d indicates the LTT-LTO phase transition pressure.

Fig. 118. Pressure dependence of T_m and T_c for LBCO with $x = 0.135$. P_d indicates the LTT-LTO phase transition pressure.

Experiment 951
Magnetism and flux line lattice structure of oxychloride superconductors
(K. Ohishi, R. Kadono, KEK-IMSS)

The $Ca_{2-x}Na_xCuO_2Cl_2$ (Na-CCOC) compounds used in this study were synthesized under high pressure [Hiroi *et al.*, Nature **371**, 139 (1994); *ibid.*, Physica **C266**, 191 (1996)]. The samples were characterized by means of magnetization and powder X-ray diffraction. The lattice parameters were determined by using a Rietveld analysis for all samples in order to evaluate the sodium concentration dependence of the lattice parameters. The ZF-μSR measurements were conducted at TRIUMF and at the Muon Science Laboratory, High Energy Accelerator Research Organization (KEK-MSL). We prepared eleven sets of Na-CCOC polycrystalline specimens, $x = 0$, 0.0025, 0.005, 0.01, 0.02, 0.05, 0.07, 0.10, 0.12, 0.15, and 0.20, having a dimension of about $100 \sim 250$ mm^2 with ~ 1 mm thickness. These samples were mounted on a thick silver sample holder (KEK-MSL) or on a thin sheet of mylar film (TRIUMF, where one can obtain background free spectra) and loaded to the ^{4}He gas flow cryostat. ZF-μSR measurements were mainly performed at temperatures between 2 K and room temperature, and additional measurements were performed at ambient temperature under a transverse field ($\simeq 2$ mT) to calibrate the instrumental asymmetry. The dynamics of local magnetic fields at the muon sites was investigated by longitudinal field (LF)-μSR measurements [Schenck, *Muon Spin Rotation: Principles and Applications in Solid State Physics* (Adam Hilger, Bristol, 1986)].
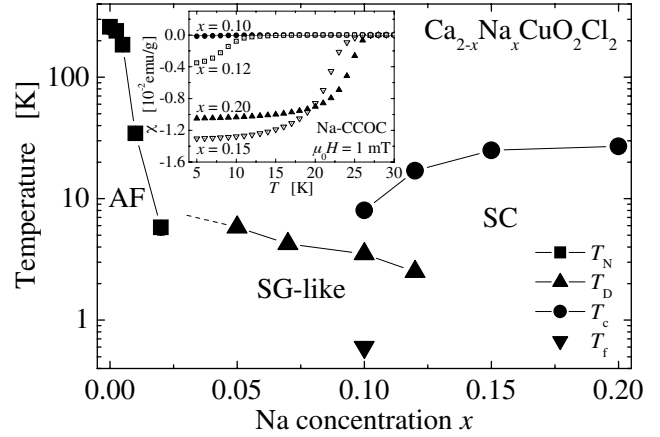

Fig. 119. Magnetic phase diagram of Na-CCOC. The transition temperature for the SG-like state (T_D) is defined as an onset temperature where the spin fluctuation rate becomes lower than 10^9 s^{-1}. The spin freezing temperature (T_f) was determined only for $x = 0.10$. The inset shows the temperature dependence of magnetic susceptibility measured for $x = 0.10$, 0.12, 0.15 and 0.20 in an applied field $\mu_0 H = 1$ mT after field-cooling process.

Figure 119 shows the magnetic phase diagram of Na-CCOC ($0 \leq x \leq 0.20$) determined by μSR measurements. As we reported in last year's Annual Report, we have observed clear muon spin precession signals in the lightly doped samples ($x \leq 0.02$), indicating the appearance of a long range antiferromagnetic (AF) order. While no precession signal was identified in those with $0.05 \leq x \leq 0.12$, evidence was found for a quasi-static spin glass(SG)-like state at lower temperatures. It suggests a general trend that the suppression of long range AF order is strong but incomplete over the relevant range of sodium concentration. In particular, the present result is the first example for a good correspondence between such an inhomogeneous magnetic state and the nanoscale electronic inhomogeneity revealed by STM/STS [Kohsaka *et al.*, Phys. Rev. Lett. **93**, 097004 (2004); Hanaguri *et al.*, Nature **430**, 1001 (2004)]. ZF-μSR time spectra in the specimen with $x = 0.15$ and 0.20 exhibit the least temperature dependence down to 2 K. Besides the signature of the static nuclear magnetic moments described by the Kubo-Toyabe function, we obtained no evidence for any kind of additional magnetic moments in the specimen with $x = 0.15$ and 0.20.

In summary, our μSR measurements on Na-CCOC revealed a magnetic phase diagram as a function of carrier doping x, which shares many features in common with other hole-doped cuprates [Niedermayer *et al.*, Phys. Rev. Lett. **80**, 3843 (1998)]. The AF order observed in the sample with $0 \leq x \leq 0.02$ is drastically suppressed in those with $x > 0.02$. However, the suppression is incomplete so that a SG-like phase appears over a region $0.05 \leq x \leq 0.12$. The present result

strongly suggests that the inhomogeneous magnetic state commonly found in the underdoped cuprates has an intrinsic origin related to the nanoscale electronic inhomogeneity observed by STM/STS measurements.

Experiment 960
Hydrogen (Mu) defects in II-VI chalcogenides
(R.L. Lichti, Texas Tech; J.M. Gil, Coimbra)

In this run, we focused our attention on the compound ZnSe, which is the most interesting zinc chalcogenide both from the fundamental and the technological point of view. We had previously identified, in the 2003 run, the existence of two possible Mu states in high transverse field, in two different, nominally undoped, ZnSe single crystals, obtained from Crystec and from Alpha Aesar. In this run, we have pursued the spectroscopic study of these Mu states and the respective interconversion dynamics, together with the study of the missing fraction.

Anisotropy vs. two isotropic states hypothesis

We have performed high-transverse field experiments on two other single crystals from Crystec, oriented 110 and 111, from the same batch as the 100 sample used previously. The results preclude the hypothesis that the two observed lines arise from anisotropy of a single Mu state. The existence of two isotropic Mu states in ZnSe has thus been firmly established. As pointed out previously, the obtained hyperfine interactions are consistent with those calculated theoretically by Van de Walle and Blöchl [Phys. Rev. **B47**, 4244 (1993)], suggesting that the observed states are located in the tetrahedral interstitial sites. Thus, the signal (Mu_I) with hyperfine interaction $A_I = 3423.99$ MHz is tentatively assigned the T_{Zn} location and the signal (Mu_{II}) with hyperfine interaction $A_{II} = 3255.3$ MHz is tentatively assigned the T_{Se} location.

Detailed study of the interconversion of the states

We have performed a detailed temperature scan at a high transverse field (6 T), in order to investigate the thermal stability of both states. A single crystal of ZnSe obtained from Alpha-Aesar, nominally undoped, was used. We have verified the conversion of one of the states (named Mu_{II}) to the other (Mu_I) at around 50 K. This conversion is accompanied by a characteristic peak in the phase of the frequency of Mu_I (shown in Fig. 120), together with an increase of the relaxation rate of Mu_{II}. Above 50 K, only the Mu_I line is seen up to 300 K, with a temperature dependent formation probability (Fig. 121).

Missing fraction

We have also undertaken studies in high longitudinal fields in order to investigate the behaviour of the observed missing fraction. The data are well described
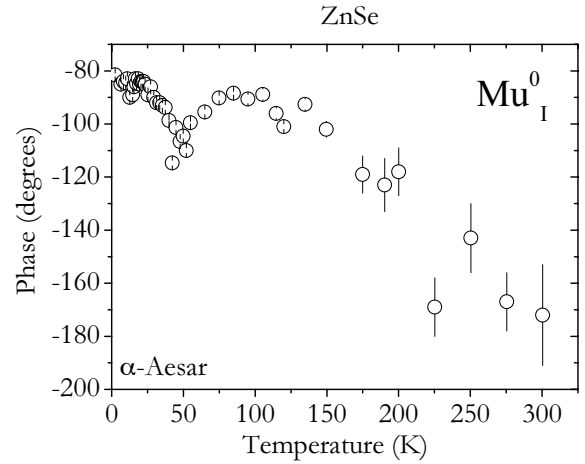

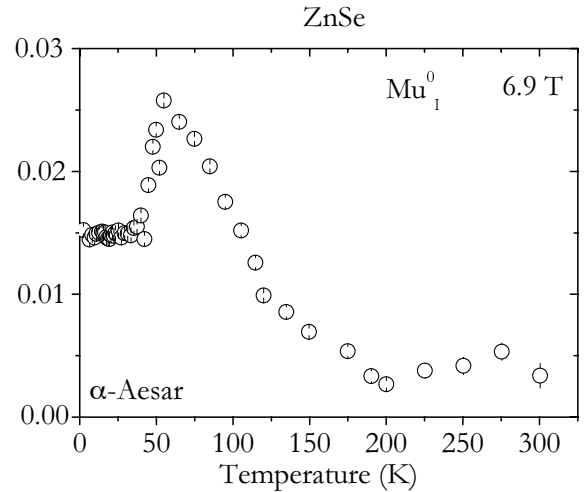Fig. 120. Phase of the Mu_I frequency, peaking at about 50 K.

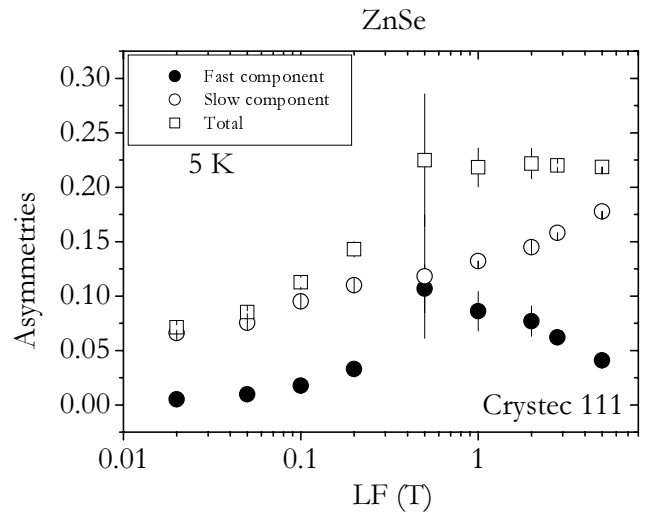Fig. 121. Asymmetry of the Mu_I state as a function of temperature.

Fig. 122. Asymmetry dependence with longitudinal field for the two components observed in the Crystec 111 ZnSe sample, at 5 K.
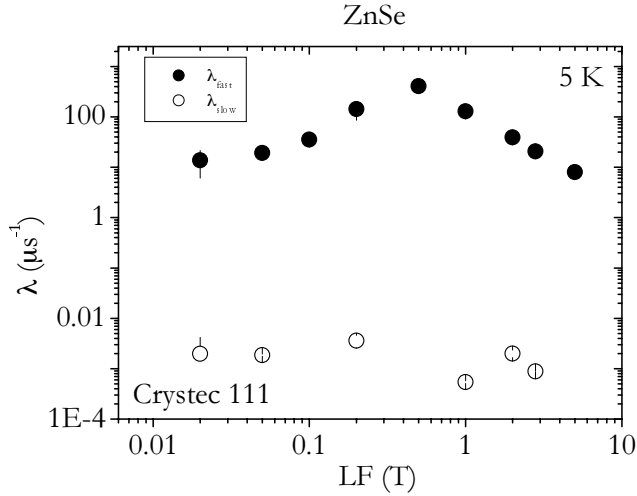
Fig. 123. Relaxation rate dependence with longitudinal field for the two components observed in the Crystec 111 ZnSe sample, at 5 K.

with two-component fits, where an extremely fast relaxation component is superimposed to an almost non-relaxing component. The corresponding asymmetries and relaxation rates at 5 K are depicted in Figs. 122 and 123, respectively. As illustrated in these figures, full asymmetry is recovered at low temperatures, the TF missing fraction corresponding to the fast relaxing component observed in LF.

Experiment 998
Muon spin relaxation and dynamic scaling in novel magnetic materials
(D.E. MacLaughlin, California, Riverside; R.H. Heffner, JAERI-ASRC)

Magnetic materials provide flexible and universal systems in which to study the dynamics of interacting electron spins. Critical behaviour is a well-known example that has been fairly well characterized for simple ferromagnets and antiferromagnets, but less is known about exotic quantum, glassy, and frustrated spin systems, in which spin fluctuations are slowed significantly. We have begun μSR experiments to study spin dynamics in a number of such systems.

μSR is a low-frequency probe of spin dynamics and hence is particularly sensitive to slow spin fluctuations. It is therefore ideally suited to studies of long-lived spin correlations in these novel spin systems. Under certain conditions, the muon spin relaxation function $G(t, H)$ can be shown to obey the time-field scaling relation $G(t, H) = G(t/H^y)$, where y is related to the form of the spin correlation function and low-frequency divergences in the fluctuation spectrum. In the case of critical fluctuations near a phase transition, this in turn gives information on the dynamical scaling exponent z.

In 2004, μSR experiments were carried out to study slow spin dynamics in the non-Fermi-liquid (NFL) heavy-fermion alloy $Ce_{0.2}La_{0.8}RhIn_5$ and geometrically frustrated antiferromagnet $Gd_2Ti_2O_7$. We did not observe time-field scaling in either of these systems, and $Ce_{0.2}La_{0.8}RhIn_5$ showed no evidence at all for slow fluctuations. The results are interesting in their own right, however, as described below. Papers on both these experiments are currently in preparation.

Spin freezing and non-glassy dynamics in $Ce_{0.2}La_{0.8}RhIn_5$

Specific heat and magnetization studies of the $Ce_{1-x}La_xRhIn_5$ alloy series give evidence for the Griffiths-phase theory disorder-driven NFL behaviour of Castro Neto and co-workers. In this picture quantum tunneling of RKKY-coupled local-moment clusters dominate the low-temperature properties of the system. Our zero-field muon spin relaxation (μSR) experiments on $Ce_{0.2}La_{0.8}RhIn_5$ show that this alloy exhibits disordered spin freezing with a sharp transition at 0.16 K, and thus does not remain a paramagnetic metal, NFL or Fermi-liquid, as $T \to 0$.

Figure 124 shows the evolution of the zero-field muon spin relaxation from high-temperature Kubo-Toyabe behaviour due to nuclear dipolar fields to faster relaxation as $T \to 0$. This behaviour is well fit by an exponentially damped Kubo-Toyabe function. The temperature dependence of the exponential rate is given in Fig. 125, where it can be seen that a sudden onset occurs at $T = 0.16$ K. Assuming that this additional relaxation is due to a static distribution of local fields, the frozen moment at $T = 0$ is estimated as ~ 0.13 μ_B/Ce ion. This is an order of magnitude smaller than found from thermodynamic data, which indicates substantial compensation of the local moments by a Kondo effect with a characteristic temperature considerably higher than the freezing temperature.

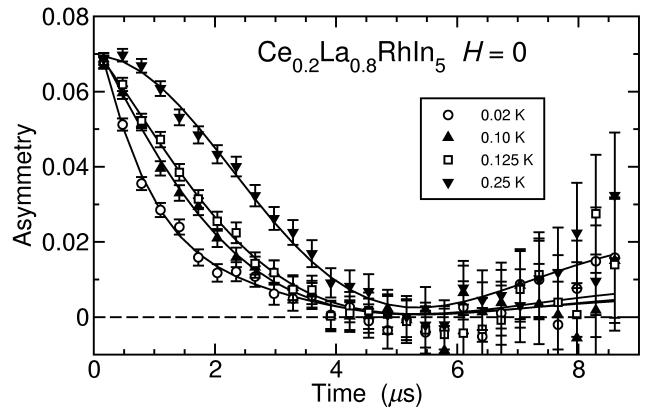That the zero-field relaxation is indeed static is indicated by the behaviour of the longitudinal-field μSR

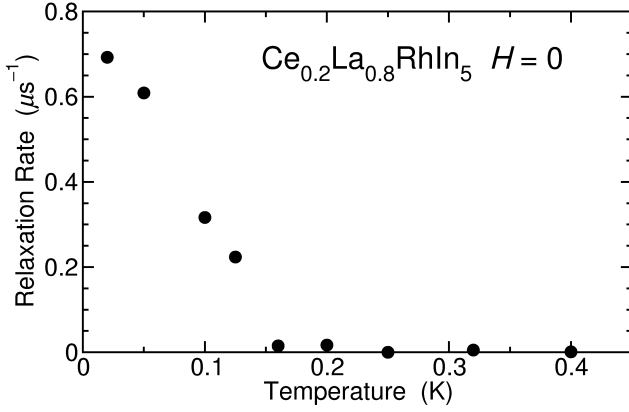Fig. 124. Zero-field μSR asymmetry functions in $Ce_{0.2}La_{0.8}RhIn_5$.

Fig. 125. Temperature dependence of the exponential muon spin relaxation rate in $Ce_{0.2}La_{0.8}RhIn_5$, $H = 0$.
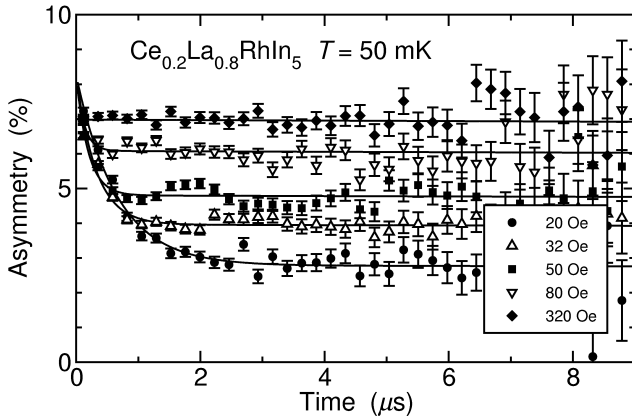

Fig. 126. Longitudinal-field muon spin relaxation functions at $T = 50$ mK in $Ce_{0.2}La_{0.8}RhIn_5$.

shown in Fig. 126, where it can be seen that the relaxation of the long-time component is extremely slow and the applied field decouples the relaxation. No dynamic relaxation is observed at any temperature; the spin freezing is not accompanied by the slow spin fluctuations found in spin glasses above the glass temperature and in a number of disordered NFL systems. This suggests that the freezing process never generates slow spin fluctuations, which seems inconsistent with the Griffiths-phase model.

Field dependence of critical slowing down in the frustrated pyrochlore $Gd_2Ti_2O_7$

In the pyrochlore titanate $Gd_2Ti_2O_7$ the Gd^{3+} local moments occupy corner-shared tetrahedra, leading to geometrical frustration, enormous ground-state degeneracy, and extreme sensitivity to mechanisms that break this degeneracy. $Gd_2Ti_2O_7$ exhibits a magnetic phase transition around 1 K, and a complex field-temperature phase diagram is found below this temperature. The 1 K transition is depressed slightly with field, and at $\sim$2.5 T and $\sim$0.86 K a pentacritical point is observed.
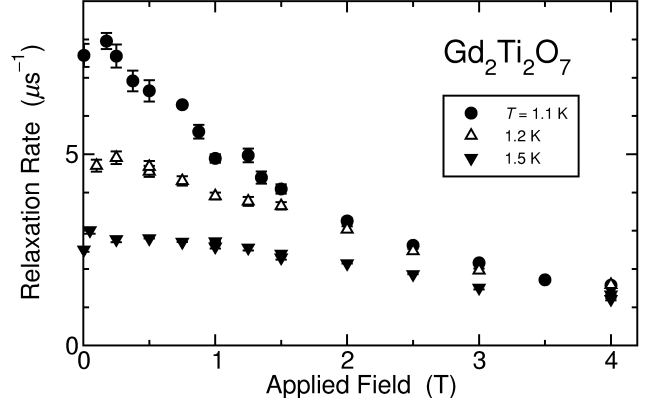

Fig. 127. Field dependence of the longitudinal-field muon spin relaxation rate in $Gd_2Ti_2O_7$.

We have carried out LF-μSR in $Gd_2Ti_2O_7$ at temperatures just above the phase transition in longitudinal fields of up to 4 T. As can be seen in Fig. 127, at low fields the exponential relaxation rate increases markedly as the freezing temperature is approached from above. Similar behaviour is often observed in the neighbourhood of a magnetic transition, and is interpreted as evidence for critical slowing down of the spin fluctuations. In this case the rate increase is suppressed by applied field. This is surprising if the high- and low-temperature phases are separated by a line of second-order phase transitions, since then there should be critical slowing down at any applied field as the transition line is approached.

Our results suggest that only the zero-field transition is of second order, a situation that is reminiscent of ferromagnetism (which of course has no transition in nonzero field), and that to our knowledge has not been anticipated theoretically. No relaxation-rate anomaly is seen in the neighbourhood of the pentacritical point at $\sim$2.5 T even at the lowest temperatures.

Experiment 1000
Measurements of the vortex core size in type-II superconductors
(J.E. Sonier, F.D. Callaghan, SFU)

Muon spin rotation (μSR) has emerged as the leading experimental probe of the effective size of magnetic vortices in type-II superconductors. μSR data on several different classes of type-II superconductors show that the size of the vortex core can depend quite strongly on temperature and the strength of the external magnetic field. These behaviours are attributable to the quasiparticle excitation spectrum both inside and outside of the vortex cores. Recently, we clearly demonstrated that the vortex-core size in the conventional superconductor V_3Si changes as a function of magnetic field due to the intervortex transfer of quasiparticles [Sonier *et al.*, Phys. Rev. Lett. **93**, 017002 (2004)]. The result confirms a key prediction of recent
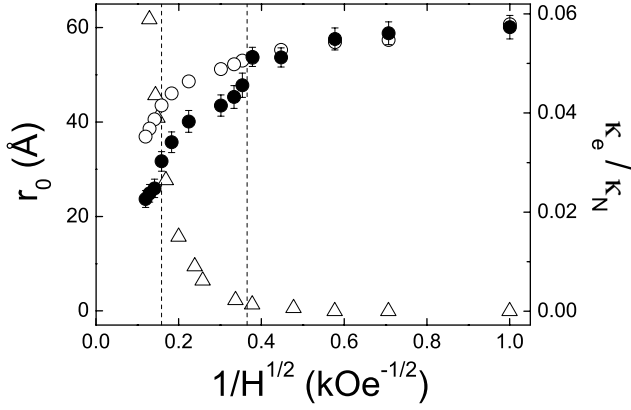
Fig. 128. The magnetic field dependence of the vortex core size r_0 measured by μSR (solid circles) at $T = 3.8$ K from Sonier *et al.* [*op. cit.*], and the electronic thermal conductivity κ_e/T (open triangles) from Boaknin *et al.* [Phys. Rev. Lett. **90**, 117003 (2003)]. The open circles indicate the reduction of r_0 due only to the superposition of spatial current density profiles from individual vortices, and not the delocalization of vortex bound states. The data are plotted as a function of $1/H^{1/2}$, which is proportional to the inter-vortex spacing. The dashed vertical lines indicate the field range over which the vortex lattice undergoes a continuous hexagonal-square transition.

microscopic theories for strongly interacting vortices (Fig. 128). The effects of vortex-vortex interactions on the magnetic and electronic structure of the vortex state are of crucial importance to the interpretation of experiments on both conventional and exotic superconductors in an applied magnetic field.

The aim of Expt. 1000 is to apply our present understanding of quasiparticle core states in conventional superconductors to the investigation of the vortex-core size in unconventional type-II superconductors – keeping in mind that comparatively little is known about the structure of vortices in many of the exotic superconductors, including high-temperature cuprates. From theoretical considerations, one expects the electronic structure of a vortex to be strongly influenced by anisotropy of the superconducting energy gap, and anisotropy of the Fermi surface. With the discovery of MgB$_2$ has come particular interest in the effects of multi-band superconductivity (MBSC) on vortex structure. The presence of different superconducting gaps on separate Fermi sheets may lead to abnormally large vortices at low temperatures and magnetic fields. Such multi-band effects appear to be important in a number of type-II superconductors. This includes NbSe$_2$, and even the high-temperature superconductor YBa$_2$Cu$_3$O$_{7-\delta}$.

In 2004 we carried out transverse-field μSR measurements on several type-II superconductors. The determination of the vortex-core size from these measurements requires extensive data analysis. A considerable amount of time was spent this past year writing a

more powerful analysis code that takes full advantage of today's high-speed computers. Very recently we have completed our anlaysis of low-temperature data for the multi-band superconductor NbSe$_2$.

The measurements on NbSe$_2$ were performed in a dilution refrigerator at $T = 20$ mK. Such low temperatures suppress thermal excitations of the electronic vortex core states, which tend to obscure the effects of MBSC on the field-dependence of the core size. The results of our data analysis are presented in Fig. 129. We see that ξ (the Ginzburg-Landau coherence length, which is a measure of the vortex core size) decreases rapidly at low fields before saturating at $H \approx 5$ kOe. The rapid shrinkage at low field is due to the more extended nature of the loosely bound core states associated with the smallest energy gap. This leads to rapid quasiparticle delocalization, as evidenced by the rapid increase in electronic thermal conductivity in the same field range. This behaviour is consistent with recent theoretical calculations of the local density of states in a multi-band superconductor. The rapid suppression of core states associated with the smaller energy gap means that the behaviour of the core size above 5 kOe is determined solely by the larger gap. The observed field-independent behaviour of the core size for 5 kOe $\geq H \leq 16$ kOe indicates no significant delocalization of core states associated with the large gap in this field range.

We have also established a direct relationship between the vortex core size and the electronic thermal conductivity in both single-band and multi-band type-II superconductors. In the conventional picture of an
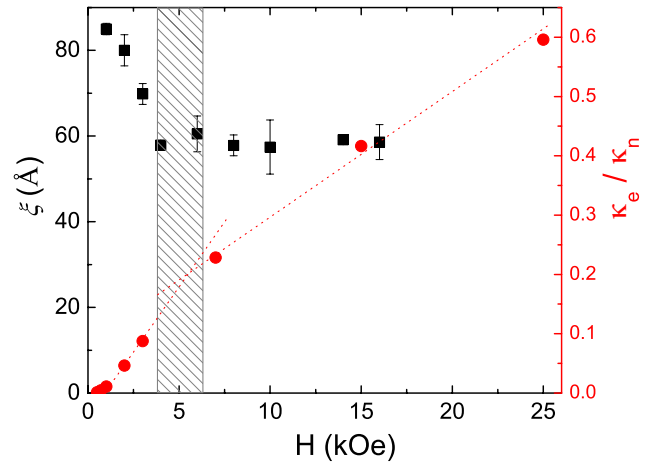

Fig. 129. The magnetic field dependence of the vortex core size ξ measured by μSR (solid squares) at $T = 20$ mK, and the electronic thermal conductivity κ_e/T (solid circles) from Boaknin *et al.* [*op. cit.*]. The dashed line is a guide for the eye. The shaded region indicates the field range in which the form of the field-dependence of both quantities changes due to the multi-band nature of the superconductivity in this material.
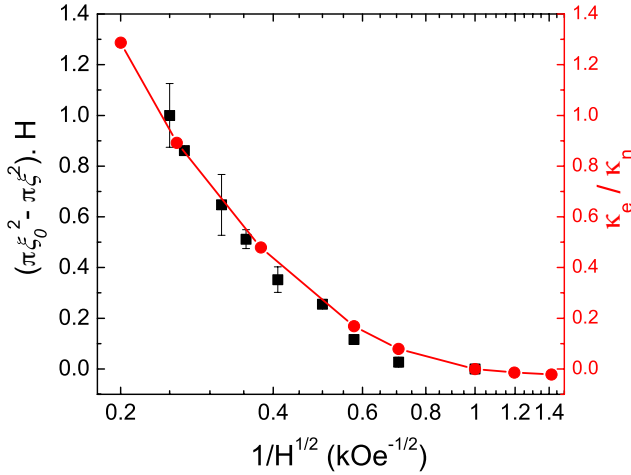
Fig. 130. The total reduction in core area (left axis, solid squares) and the electronic thermal conductivity (right axis, solid cirles) for NbSe$_2$ plotted against $1/\sqrt{H}$ which is proportional to the intervortex spacing.

s-wave type-II superconductor, the density of bound core states is proportional to the vortex core area. Extending this to the scenario of a field-dependent core size, we have shown that the electronic thermal conductivity is directly proportional to the field-induced reduction in core area in the sample ($\sim(\pi\xi_0^2 - \pi\xi^2)\cdot H$, where ξ_0 is the measured low-field value of the coherence length). This is demonstrated in Fig. 130 where we plot both quantities for NbSe$_2$ against $1/\sqrt{H}$ (which is proportional to the intervortex spacing). For both materials the two data sets show the same field-dependence. This agreement is also observed in V$_3$Si. Coupled with earlier work [Sonier *et al.*, Phys. Rev. Lett. **82**, 4914 (1999)] that established the effect of core size on the specific heat of NbSe$_2$, we have now established an intimate relationship between the vortex core size and the thermal properties of s-wave type-II superconductors.

Experiment 1001
Mu defect levels in III-V semiconductors
(R.L. Lichti, Texas Tech)

The main experimental goal of Expt. 1001 is to accurately measure ionization rates for the bond-centred (BC) and tetrahedral (T) muonium species in III-V compounds in order to determine the muonium analogue of the donor and acceptor defect energy levels for hydrogen impurities in these compounds. If both of these defect levels fall within the bandgap, their midpoint locates the primary hydrogen level that has been predicted to be pinned at a universal energy with respect to vacuum, independent of the host material [Van de Walle and Neugebauer, Nature **423**, 625 (2003)]. The purpose of this experiment is to test these predictions and locate that energy as accurately as pos-

sible for materials where the neutral charge state of Mu is observed for both the BC (donor) and T (acceptor) sites. Both Mu^0 centres are well known to occur in GaAs and GaP; however, previous data did not provide any of the required ionization energies to sufficient accuracy.

During the first week of beam time for this experiment, we have concentrated on obtaining the Mu donor energy level in GaAs and GaP by obtaining the ionization energy for Mu$_{BC}^0$. This is best done by extracting the lifetime broadening from the relaxation rate for the hyperfine lines for that species in spin-precession measurements. We used the HiTime apparatus, taking spectra at 5 T with relatively small temperature steps across the region where the spectra for Mu$_{BC}^0$ was known to disappear. We chose to apply the field along a $\langle 111 \rangle$ direction where one set of BC hyperfine lines is for a single bond orientation. In fact, for GaAs we were able to use all of the lines even though the field was not precisely aligned.

Figure 131 shows the activated part of the relaxation rates for a semi-insulating GaAs sample, separately extracted for each BC ($0°$) line and each set of slightly misaligned $70°$ lines. These data yield an ionization energy of 165 ± 6 meV for Mu$_{BC}^0$ in GaAs from an average of the four separate measurements. A similar treatment gives about 150 meV for Mu$_{BC}^0$ in GaP, although a final analysis of that data is not yet completed. Figure 132 shows the preliminary analysis for one of the BC hyperfine lines in a semi-insulating sample of GaP. Assuming that the BC site lies lowest in energy for Mu^0 and the disappearance is due to
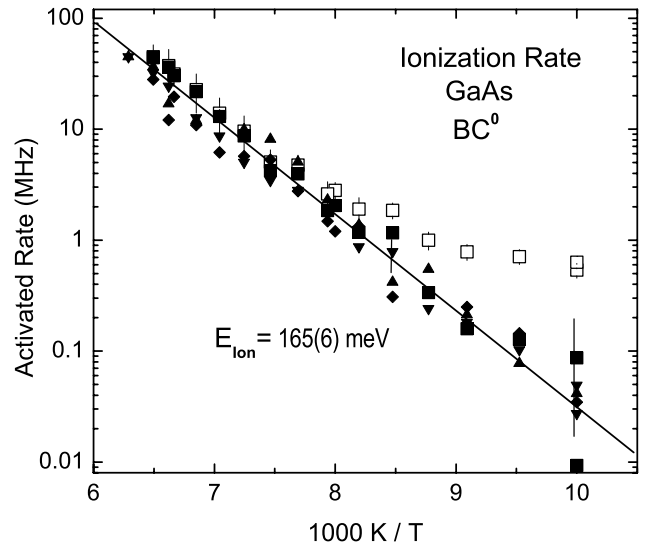

Fig. 131. Ionization rate for Mu$_{BC}^0$ in GaAs extracted from the relaxation rates for the various lines in the BC hyperfine spin-precession signals. Open squares are the raw data for one line, filled symbols have the non-lifetime contributions removed.
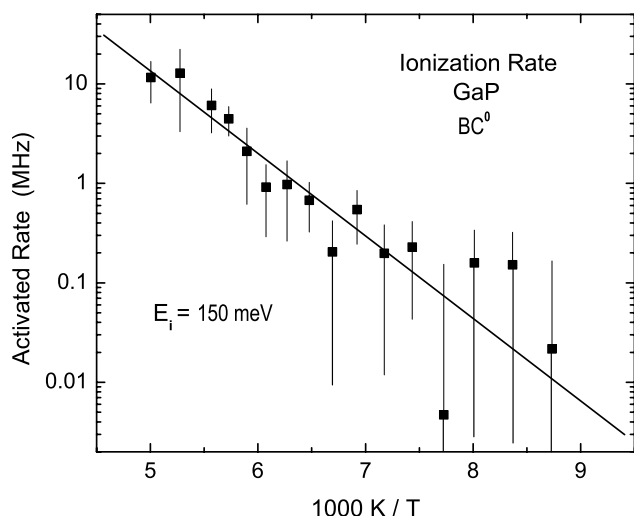
92

Fig. 132. Preliminary result for the ionization rate of Mu^0_{BC} in GaP from one of the BC hyperfine lines.

ionization via thermal promotion of an electron to the conduction band, these numbers accurately define the Mu donor level in GaAs and GaP, providing half the information required to experimentally define the hydrogen pinning energy in each case.

The energy for the Mu^0_T transition to Mu^- via "hole ionization" (promotion of an electron from the valence band onto the T-site Mu species) would yield the acceptor energy level as the other half of the necessary experimental information. The initial data imply that, in the semi-insulating GaP sample used for the BC result, the Mu^0_T signal persists to above the upper temperature limit for the HiTime spectrometer. The lower temperature data that were acquired indicate that the atomic muonium centre may be localized at a single T-site in GaP near 100 K, while in GaAs this centre is very mobile at all temperatures. There may also be a second atomic-like Mu^0 signal in GaP in addition to the Mu^0_T spectra previously reported. Specifically, between roughly 15 and 90 K a new and very narrow isotropic Mu^0 signal was observed with a HF constant roughly 250 MHz lower than that reported for Mu^0_T. The origin of this signal is not identified at this point and the nature of this new paramagnetic muonium state in GaP will be pursued in future experiments, in addition to obtaining accurate ionization energies for the standard Mu^0_T centres in both GaAs and GaP.

Experiment 1012
Organic free radicals under hydrothermal conditions
(P.W. Percival, SFU)

Research on organic chemistry under hydrothermal conditions is motivated by many different applications, including geochemical production of fossil fuels, biology of submarine volcanic vents, corrosion in pressur-

ized water nuclear reactors, destruction of chemical weapons and other hazardous materials, and "green" industrial processes. However, fundamental investigations of chemical reactions require the detection and monitoring of intermediates, often transient free radicals, which are difficult to detect under the extremes of pressure and temperature that define near critical and supercritical aqueous systems. In Expt. 842 we demonstrated the ability to study chemistry in aqueous systems up to 400°C and 400 bar, and in last year's Annual Report we reported the first muon level-crossing spectra of muoniated free radicals under such conditions. Experiment 1012 was specifically designed to capitalize on this success, and to apply the combination of transverse-field μSR and level-crossing spectroscopy to investigate organic free radical chemistry in superheated water. To date we have explored applications in two areas: dehydration of alcohols and the enolization of acetone. The radicals detected, and their means of generation in superheated water, are listed in Fig. 133.

Examples of spectra are shown in Fig. 134 for the 2-propyl radical. The muon hyperfine constant is readily determined from the transverse-field μSR spectrum, being the difference between the two radical precession frequencies, as indicated by the double-headed arrow. The proton hyperfine constants can then be calculated from the μLCR resonance fields. There are three chemically distinct H atoms in 2-propyl, and this gives rise to three resonances, of which two are close enough to overlap. The hyperfine constants are sufficient to confirm the identification of the radicals produced in various chemical systems. For example, 2-propyl was identified as a product of the dehydration of both 2-propanol
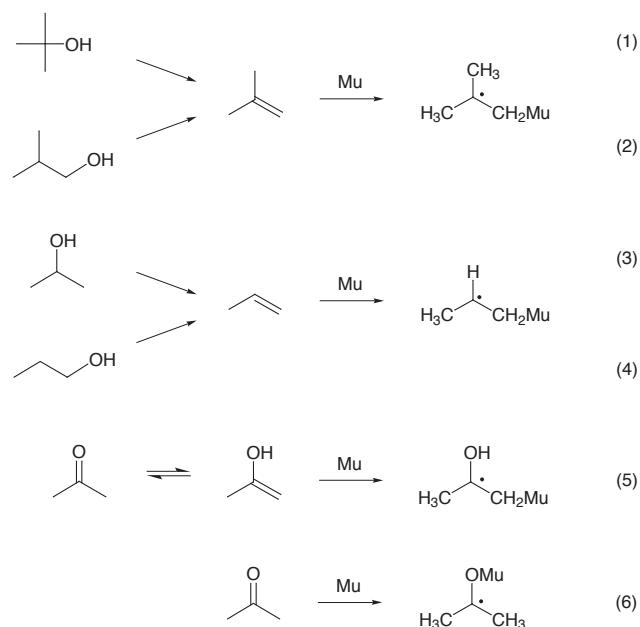

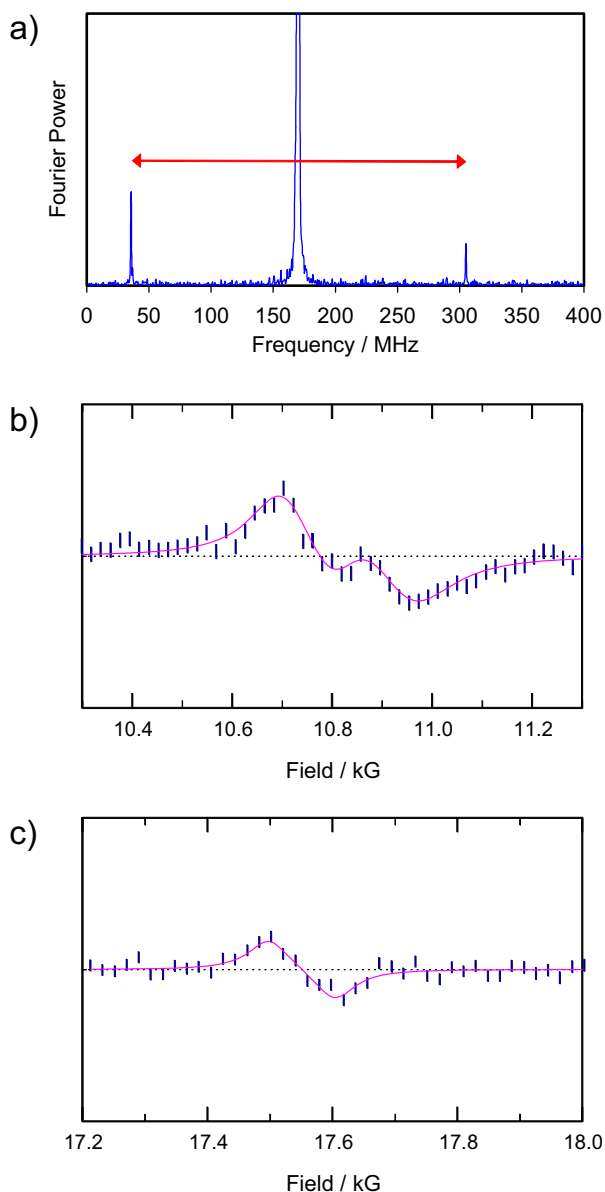Fig. 133. Generation of muoniated radicals in superheated water.

93

Fig. 134. Muon spectra of the 2-propyl radical in water at 350°C: (a) TF-μSR spectrum, (b) CH$_3$ and CH$_2$Mu resonances from the μLCR spectrum, and (c) α-H resonance.

and 1-propanol. A summary of muon and proton hyperfine constants, and their assignments, is given in Table XVI.

Sometimes identification of the radical intermediate is sufficient to resolve a particular question, such as the detailed mechanism of a reaction. In other cases the radical may merely play the role of a useful, identifiable "marker". For example, the *keto-enol* tautomerism of acetone may be investigated by "labelling" the isomeric molecular forms as indicated in reactions (5) and (6) of Fig. 133.

Yet a third class of investigation involves the properties of the muoniated radical itself. By analyzing the temperature dependence of free radical hyperfine con-

stants it is possible to deduce details of intramolecular motion as well as potential interactions with the solvent. We emphasize that there is currently *no other technique available* to study organic free radicals under hydrothermal conditions. The subject of our first detailed study is the *tert*-butyl radical, which we have previously studied at much lower temperatures in organic media [Percival *et al.*, Chem. Phys. **127**, 137 (1988)]. Our new data are summarized in Fig. 135. Consistent with the earlier study, we find that the muon hyperfine constant falls with temperature and that this is matched by an increase in one of the proton hyperfine constants. To aid comparison, a reduced muon hyperfine constant is defined, $A'_\mu = 0.31413A_\mu$, to account for the ratio of proton to muon magnetic moments. It is then possible to calculate an average hyperfine constant for the CH$_2$Mu group: $(A'_\mu + 2A_p)/3$. As is evident from Fig. 135 this quantity is essentially temperature-independent, indicating that the temperature dependence of the separate muon and proton hyperfine constants is due to the rotational motion of the CH$_2$Mu group about a C–C bond. The second proton hyperfine constant is also temperature invariant, consistent with its assignment to the CH$_3$ groups, whose C_3 symmetry results in an average value regardless of the motion. Detailed modelling of the results should provide the potential barrier for CH$_2$Mu rotation.
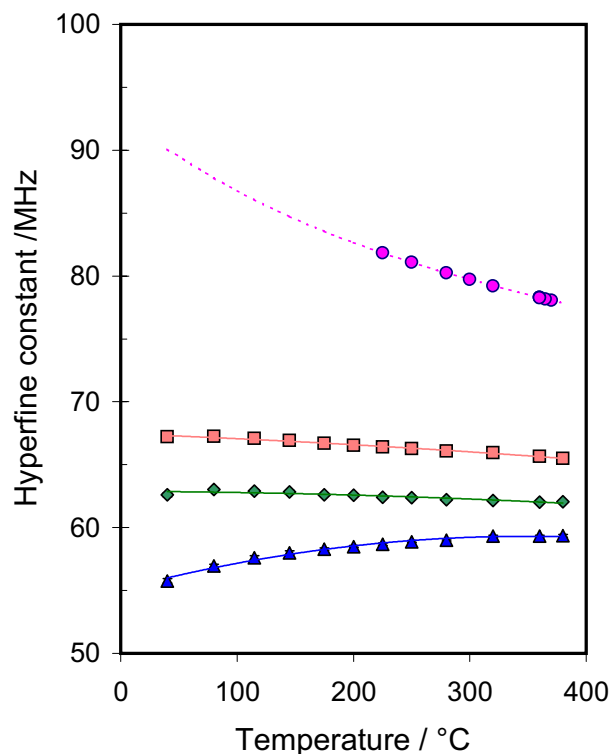

Fig. 135. Hyperfine constants for *tert*-butyl in water: ∘ reduced muon constant (from CH$_2$Mu), ◇ proton constant from CH$_3$, △ proton constant from CH$_2$Mu, □ average for the CH$_2$Mu group.

Table XVI. Assignments and hyperfine constants for muoniated radicals detected in aqueous solutions of organic compounds at high temperature.

Sample	Radical	$T/°C$	$P/$bar	$B_{LCR}/$kG	$A_\mu/$MHz	$A_p/$MHz	Assignment
1 M t-BuOH	$(CH_3)_2\dot{C}CH_2Mu$	250	250	10.47	258.14	62.4	CH_3
		250	250	10.66	249.95	59.8	CH_2Mu
0.01 M t-BuOH	$(CH_3)_2\dot{C}CH_2Mu$	350	260	10.03	249.95	62.4	CH_3
		350	260	10.17	249.95	59.8	CH_2Mu
0.7 M i-BuOH	$(CH_3)_2\dot{C}CH_2Mu$	350	260	10.03	249.95	62.4	CH_3
		350	260	10.18	249.95	59.7	CH_2Mu
1 M 2-PrOH	$CH_3\dot{C}HCH_2Mu$	350	258	10.76	269.3	68.1	CH_3
		350	258	10.91	269.3	65.4	CH_2Mu
1 M 1-PrOH	$CH_3\dot{C}HCH_2Mu$	350	251	10.75	269.3	68.2	CH_3
		350	251	10.91	269.3	65.4	CH_2Mu
		350	240	17.55	269.3	–57.7	α-H

Experiment 1013
Superconductivity of β-pyrochlore oxides
(A. Koda, R. Kadono, KEK)

Very recently, it was revealed that KOs_2O_6, having a β-pyrochlore structure, exhibits a bulk superconductivity below $T_c \simeq 9.6$ K [Yonezawa *et al.*, J. Phys. Cond. Matter **16**, L9 (2004)]. Subsequently, a series of β-pyrochlore superconductors, $RbOs_2O_6$ ($T_c \simeq 6.3$ K) and $CsOs_2O_6$ ($T_c \simeq 3.3$ K), were discovered [Yonezawa *et al.*, J. Phys. Soc. Jpn. **73**, 819 (2004); *ibid.*, J. Phys. Soc. Jpn. **73**, 1655 (2004).] In the β-pyrochlore structure, it is notable that the formal oxidation state of the Os ion is 5.5+ ($5d^{2.5}$). Such a mixed valence state has scarcely been studied in pyrochlore oxides so far, because of difficulty in the crystal synthesis. Another intriguing aspect is that the superconductivity occurs under a geometrically frustrated condition. This is in marked contrast to the case of $Cd_2Re_2O_7$ which has been the only pyrochlore oxide known as a superconductor until the discoveries of β-pyrochlore superconductors; the superconductivity in $Cd_2Re_2O_7$ occurs after a structural phase transition which is presumed to lift the degeneracy due to the geometrical frustration. Thus, there is an interesting possibility that the superconductivity in β-pyrochlore oxides might be realized on the spin-liquid ground state, as predicted for the triangular lattice by Anderson a long time ago. In order to obtain the clue to the pairing mechanism of superconductivity on pyrochlore lattice, we have conducted μSR measurements on KOs_2O_6 under a high transverse field.

In Fig. 136, the temperature dependence of the transverse relaxation rate (σ) of KOs_2O_6 at $B = 2$ T is shown. According to the Gorter-Casimir two-fluid model, the magnetic penetration depth λ is inversely proportional to $\sqrt{1 - (T/T_c)^4}$. From a relation $\sigma \propto \lambda^{-2}$, we obtain $\sigma \propto 1 - (T/T_c)^4$. As shown in Fig. 136,
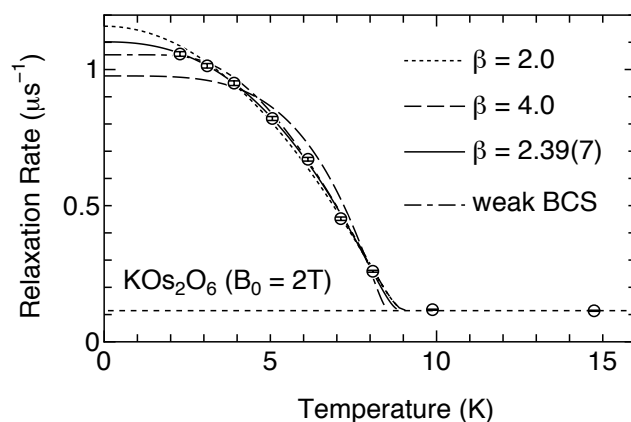

Fig. 136. Temperature dependence of transverse spin relaxation rate (σ) under a field of 2 T. The results of fitting analysis using the relation $\sigma \propto 1 - (T/T_c)^\beta$ are shown, together with the weak-coupling BCS case (dot-dashed curve). The dotted curve is for $\beta = 2$, whereas the dashed curve is for $\beta = 4$. The best fit is obtained when $\beta = 2.39$, which is represented by the solid curve.

our data exhibit significant deviation from this relation. The fitting analysis was then made with an arbitrary power,

$$\sigma = \sigma(T = 0)\left[1 - \left(\frac{T}{T_c}\right)^\beta\right],$$

with T_c as a free parameter. Here, the contribution from the nuclear magnetic moments like ^{39}K and ^{189}Os seen at $T > T_c$ was subtracted by a fixed amount prior to the fitting analysis. While the best fit is obtained when $\beta = 2.39(7)$ and $T_c = 8.91(3)$, the observed temperature dependence is nearly reproduced by $\beta = 2$ and $T_c = 9.07(2)$. The results are shown in Fig. 136 together with the fitting result by the weak-coupling BCS model. As seen in Fig. 136, it is quite difficult to distinguish those power-laws from the fully gapped case (weak BCS) only by analyzing the present data points above 2 K.
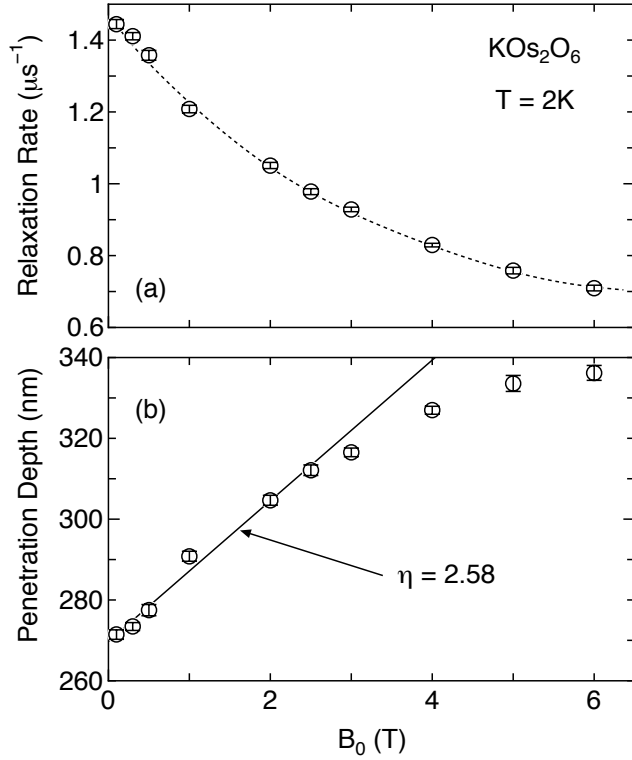
Fig. 137. Field dependence of (a) the transverse relaxation rate at 2 K and (b) the penetration depth (λ) deduced by assuming $B_{c2} = 40\,\mathrm{T}$. The broken curve in the upper panel is a guide to the eye. λ clearly obeys a linear dependence below $B \simeq 3\,\mathrm{T}$, whereas it shows a saturating tendency at higher fields. By fitting data below $2.5\,\mathrm{T}$ with the relation $\lambda = \lambda_0(1 + \eta(B/B_{c2}))$, we obtain $\eta = 2.58$.

In order to examine the low-lying quasiparticle excitations of KOs_2O_6, we measured the field dependence of λ at the lowest temperature of 2 K. In Fig. 137(a), the field dependence of σ is shown. Although the exact value of the upper critical field B_{c2} in the present specimen is unknown, we deduced λ versus the external field by assuming $B_{c2} \simeq 40\,\mathrm{T}$ as suggested by bulk measurements. As shown in Fig. 137(b), the obtained λ is clearly field-dependent, showing a slight negative curvature with respect to the applied field. In particular, an approximately linear tendency is seen below $\sim$3 T. Such increase of λ with increasing field indicates the occurrence of quasiparticle excitation due to the Doppler shift (i.e., so-called nonlinear effect) in the flux line lattice state and thereby strongly suggests the presence of low-lying quasi-particle excitations characterized by a small energy scale less than 2 K ($\simeq$0.2 meV).

It is interesting to note that the observed tendency of saturation for λ against applied field has been reported in the case of $YBa_2Cu_3O_7$, which is explained by a combination of nonlinear and nonlocal effects [Sonier *et al.*, Phys. Rev. Lett. **83**, 4156 (1999); Amin *et al.*, Phys. Rev. Lett. **84**, 5864 (2000)]. However, we cannot exclude the multiple-gap scenario in KOs_2O_6, as it has been found in MgB_2 [Ohishi *et al.*, J. Phys. Soc. Jpn. **72**, 29 (2003)], with one being a smaller energy gap than the thermal excitation energy at the temperature where the measurements were performed.

In summary, we have investigated the quasiparticle excitation in KOs_2O_6 by measuring the temperature/field dependence of λ. Our result demonstrates that λ increases markedly with applied external field up to 6 T, suggesting the presence of nonlinear and nonlocal effects. In particular, the presence of the nonlinear effect strongly suggests that the superconducting order parameter in KOs_2O_6 has a significant anisotropy or multigapped structure with a small gap energy. It is of particular interest to see whether or not the superconductivity in the other β-pyrochlore oxides is conventional.